CACTI- AND SHOREBIRDS-INSPIRED TRANSPORTS OF LIQUID DROPS AND TWO

RELATED FOG COLLECTORS

by

XIN HENG

Presented to the Faculty of the Graduate School of

The University of Texas at Arlington in Partial Fulfillment

of the Requirements

for the Degree of

DOCTOR OF PHILOSOPHY

THE UNIVERSITY OF TEXAS AT ARLINGTON

May 2015

Acknowledgements

Abstract

CACTI- AND SHOREBIRDS-INSPIRED TRANSPORTS OF LIQUID DROPS AND TWO

RELATED FOG COLLECTORS

Xin Heng, PhD

The University of Texas at Arlington, 2015

Supervising Professor: Cheng Luo

Motivated by what has been used in cacti and shorebirds to directionally manipulate water drops, we have explored two approaches to guide the movement of liquid drops. Based on these approaches, in addition to separating oil from its mixture with water, we have further developed two fog collectors.

The first fog collector has a configuration similar to its counterpart in a cactus. This collector includes a large ZnO wire and an array of small ZnO wires that are branched on the large wire. All these wires have conical shapes, whose diameters gradually increase from the tip to the root of a wire. This diameter gradient induces a capillary force to transport condensed drops from the tips to the roots of the wires. This single branched wire structure collected about 6 μL water within 30 min.

As in the case of a shorebird, the second collector employs two nonparallel plates to direct the movement of condensed drops. The two nonparallel plates are first widely opened to provide a large surface area for water vapors to condense. The condensed drops are then transported to the corner of the two plates for collection, after these drops are squeezed and relaxed using the plates. A single 10-inch by 4-inch prototype "swallowed" about a tablespoon of water in 36 minutes. Over two hours, it harvested 400-900 times more water than beetles and cacti in desert areas.

Table of Contents

List of Illustrations

x

List of Tables

Chapter 1

Introduction and Overview

1.1 Introduction

Deserts roughly cover about one quarter of the Earth's land area, and semi-deserts another quarter [1]. They have little rainfall every year. Fog and dew in some deserts may deliver more water than rainfall [1], and may be important water sources, e.g., to beetles, cacti, *dune grasses* and *cotula fallax* plants [2-5]. What these species use to collect water from fog and dew in a desert obviously provides a new insight to obtain water. It is particularly important to residents living in an arid environment, since fog and dew may always exist when temperature is deceased in late nights and early mornings.

Both capillary and gravitational forces have been employed in animals and plants to guide the movements of condensed drops through their specific surface structures. It is reported that a beetle living in the Namib Desert can collect water from fog and dew through microbumps on its back. The peaks of these microbumps are hydrophilic, while the troughs are superhydrophobic [2]. The water in the fog forms fast-growing drops on these peaks. As a drop reaches a size of 4 to 5 mm in diameter, the drop overcomes the capillary force that makes it attach to the peak, and rolls down the beetle's surface to the mouthpart [2]. It is also reported that the cactus *O. microdasys*, originated from the Chihuahua Desert, can also harvest water from the fog and dew using the spines distributed on its surface [3]. Microbarbs are grown on a spine, forming a branched wire structure. The spine may be visualized as the stem wire in the structure, while the relatively small microbarbs may be considered as branched wires. The spine and microbarb have lengths with the orders of 1 mm and 10 μm, respectively. Both spines and microbarbs have conical shapes, whose diameters gradually increase from the tip to

the root of a wire. A water drop that is condensed, e.g., on the tip of the spine or the microbarb can be driven to the root by a capillary force induced by this diameter gradient [6]. Moreover, the fog-collection behavior of the dune grasses *Stipagrostis subulicola* has been explored [4]. They use their leaves and roots to collect the fog in Namib Desert. Water drops are first condensed on leaves. When the drops become too large to be supported by the leaves, they fall to the roots, which spread over 20 m like a carpet. A similar approach is also used by *cotula fallax* plants to collect fog [5]. In addition, spider silk is found to have capability of collecting fog as well [7]. Due to a capillary force generated by the conical shape and different roughnesses of the silk surface, water drops can be guided to specific locations on the silk.

Several artificial fog collectors have been developed. They mimicked the fog-collection mechanisms of beetles and used micropeaks to collect fog [8,9-11]. On the other hand, it is considered that a hierarchical wire structure, as in the cases of cacti, *cotula fallax* plants, dune grasses and spider silk, should have higher fog-collection efficiency than micropeaks, since the hierarchical wire structure has a much larger surface area. As a matter of fact, the collection efficiency of a desert beetle has been compared with that of dune grasses *Stipagrostis subulicola* [12]. It was found that dune grasses were more efficient in harvesting fog during the same time period of 120 min in terms of both totally collected water and harvested water per unit area. It is also noted that conical-shaped copper wires have been tested in the research labs for fog collection [13]. In addition, mesh nets are also used to harvest fog [14]. A net consists of two families of intertwined fibers. Accordingly, it is a line-wise structure with each fiber visualized as a line. The fog that goes through the net holes cannot be harvested.

Furthermore, it has been reported that some feeding shorebirds with long thin beaks, such as phalaropes, are capable of driving liquid drops to move toward their

mouths by opening and closing the beaks. This process provides a new approach to control the movement of a liquid drop.

Thus, on the basis of gained understandings of the fog-collection mechanism of a cactus and feeding mechanism of a shorebird, we would like to develop two new artificial fog collectors, which could efficiently collect water from fog flow, and explore an approach to separate oil from a water/oil mixed drop using two nonparallel plates.

1.2 Dissertation Outline

First, the background and objective of the proposed research are introduced in Chapter 1. Second, a cacti-inspired collector, which is based on the branched ZnO wire structures, is presented in Chapter 2. Third, the feeding mechanism of shorebirds is introduced in Chapter 3. Fourth, a shorebird-inspired fog collector is further developed and discussed in Chapter 4. Fifth, based on the understanding of the different behaviors of liquid drops between two nonparallel plates, a new approach to separate a water/oil mixed drop is explored in Chapter 5. Finally, this work is summarized and concluded in Chapter 6.

Chapter 2

Branched ZnO Wire Structures for Water Collection Inspired by Cacti

Motivated by an approach used in a cactus to collect fog and dew, we have developed our first fog collector. This collector includes a large ZnO wire and an array of small ZnO wires that are branched on the large wire. All these wires have conical shapes, whose diameters gradually increase from the tip to the root of a wire. Accordingly, a water drop that is condensed on the tip of each wire is driven to the root by a capillary force induced by this diameter gradient. The lengths of stem and branched wires in the synthesized structures are in the orders of 1 mm and 100 μm, respectively. These dimensions are, respectively, comparable to and larger than their counterparts in the case of a cactus. Two groups of tests were conducted at relative humidity of 100% to compare the amounts of water collected by artificial and cactus structures within specific time durations of 2 and 35 s, respectively. The amount of water collected by either type of structures was in the order of 0.01 μl. However, on average, what has been collected by the artificial structures was 1.4 to 5.0 times more than that harvested by the cactus ones. We further examined the mechanism that a cactus used to absorb a collected water drop into its stem. Based on the gained understanding, we developed a setup to successfully collect about 6 μl water within 30 min.

2.1 Introduction

ZnO wires have attracted much attention in the past decade due to their specific properties of piezoelectricity, semiconductivity and wide bandgaps. They have been employed as functional components of microelectronic [15,16], optoelectronic [17-19], microfluidic devices [20], power generators [21,22], and super-hydrophobic surfaces [23,24]. They have also been applied in various sensors, such as humidity [25], gas [26], chemical [27] and biosensors [28]. The single ZnO wires reported by other researchers to

4

date only have lengths up to 300 µm [29], implying that it is an obstacle to fabricate mm-long stem wires. Moreover, different from existing ZnO wires which normally have uniform cross-sections, ZnO wires in the proposed structures should have conical shapes, which presents a second obstacle in the corresponding synthesis. These two obstacles will be specially overcome in fabricating the desired structures.

2.2 Water-collection tests on a cactus, and theoretical background

Water-collection mechanism of a cactus has been reported previously [3]. To have a better understanding about this mechanism, we also explore the cactus *Opuntiaengelmannii* var. *lindheimeri* that can be found in our campus. It has surface structures similar to what was reported for the cactus *O. microdasys* [3]. The cactus *Opuntiaengelmannii* var. *lindheimeri* also has an array of clusters on its pad surface (Fig. 2.1(a1)), and every cluster contains tens of branched wire structures (Figs. 2.1(a2) and (a3)). Both spine and microbarbs in a branched wire structure have conical shapes with apex angles of about 8° and 18°, respectively (Figs. 2.1(a4)-1(a6)). The spine has a length ranging from 0.73 to 2.43 mm, and the diameter of its middle cross-section is about 80 µm. The microbarb has a length between 18 and 50 µm, and the diameter of its middle cross-section is about 11 µm.
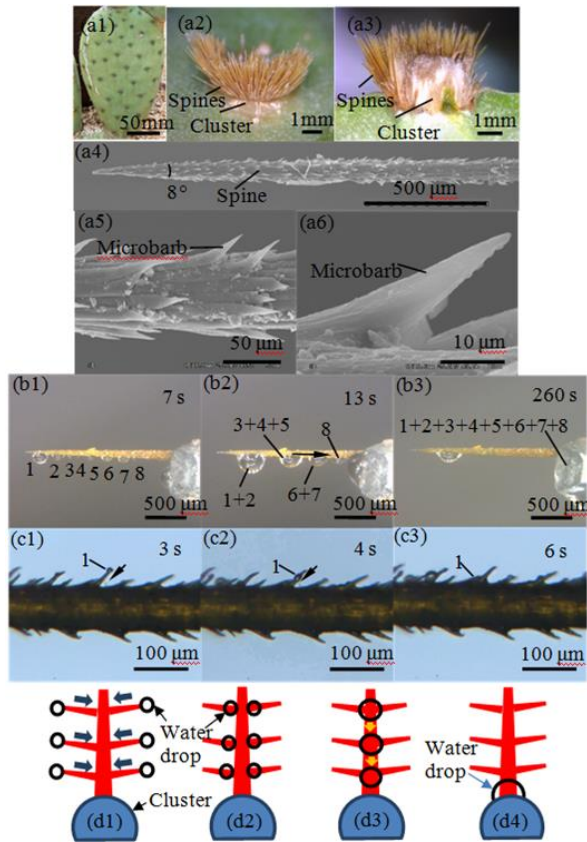
Figure 2.1 (a1) Pad of the cactus *Opuntia engelmannii* var. *lindheimeri,* whose surface is distributed with an array of clusters, (a2) side and (a3) cross-sectional views of a single cluster, which is covered by a bunch of spines. A branched wire structure, consisting of (a4) a 1.8-mm-long spine and (a5,a6) microbarbs on a cluster. (a1)-(a3) are optical images, while (a4)-(a6) are SEM ones. Water collection of a cactus through (b) a spine and (c) microbarbs. Illustration of a water-collection process of the cactus: (d1) small drops are formed on tips of branched wires, (d2) move down to the roots of these wires, and (d3) merge to form large drops, which (d4) subsequently move down to the root of the stem wire to form a larger drop. All drawings or pictures are side or top views, and numbers in (b1)-(b3) and (c1)-(c3) represent different water drops.

At room temperature (22 °C ± 1 °C), a humidifier (model: EE-5301, Crane USA Co.) was employed to generate a mist flow over a branched wire structure of the cactus *Opuntiaengelmannii* var. *lindheimeri*, which implies that relative humidity was 100% in the tested area (Fig. 2.2). The humidifier was turned on for 1 min to ensure that the flow rate was steady. Subsequently, a branched wire structure of the cactus was placed in the mist flow, followed by the recording of the water-collection process through an optical microscope. The flow was along the longitudinal direction of the branched wire structure. As shown in Figs. 2.1(b) and 2.1(c) and illustrated in Fig. 2.1(d), a representative process that a cactus collects water is as follows. A small water drop first appears on the tip of a branched wire (Figs. 2.1(d1) and 2.1(c1)), since the tips of the branched wires are directly exposed to the mist flow. There may also exist water drops on the sidewall of the branched wire. However, because this sidewall is not directly exposed to the flow, such drops may not be as large as the one on the tip. Accordingly, these drops are not found at the beginning of our test (see, for example, Fig. 2.1(c1)). Similar phenomena have been previously observed in the case of The President lotus [30]. As indicated previously [6], the small drop then moves from the tip to the root along this branched wire (Fig. 2.1(c2)). In such a manner, small water drops that are formed at the tips of the branched wires at different time instants continuously move to the roots (Figs. 2.1(d2) and 2.1(c3)). After that, they merge to form a large drop (Fig. 2.1(d3)). The large drops located on the roots of the branched wires then move to the root of the stem wire, merging over there to form a much larger drop, which is subsequently collected by the underneath cluster (Figs. 2.1(d4)) and 2.1(b)). Within 260 s, all the water drops that we specifically observed have moved to the root of the stem wire (Fig. 2.1b(3)). Repetition of this process continuously provides water into the cluster. The same procedure is subsequently used in proposed branched wire structures to collect water.
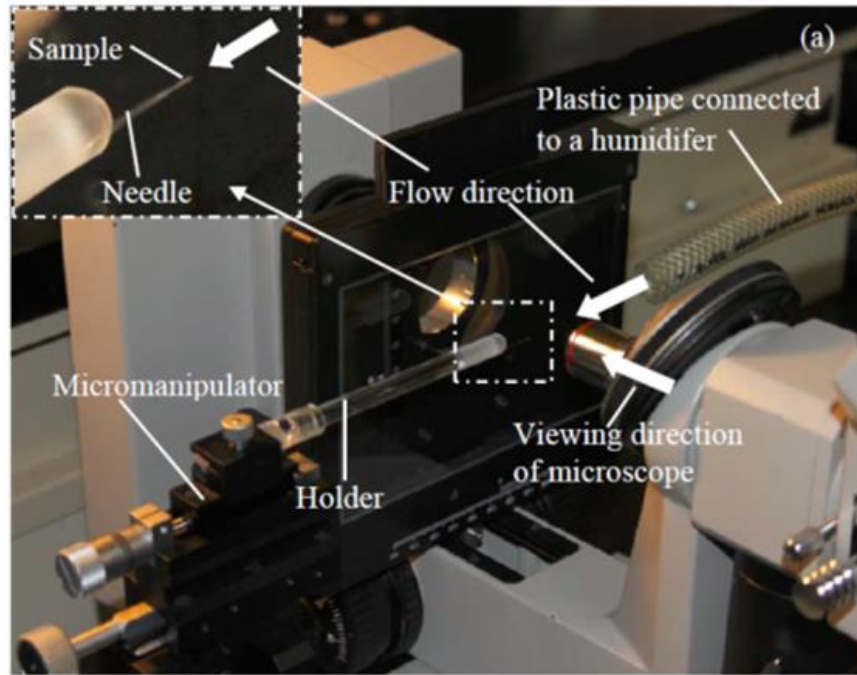
Figure 2.2 Experimental setup for water collection

A quasi-spherical liquid drop on a thin, conical wire suffers a capillary force, which has the following expression [6]:

$$dP / dz = -\gamma\theta / (r + R_0)^2, \quad\quad\quad (2.1)$$

where P denotes Laplace pressure inside a liquid drop, z the position of the drop on the wire, dP / dz Laplace pressure gradient along the wire (also representation of the capillary force), γ surface tension of the liquid, θ the apex angle, r the mean radius of the wire at the place where the drop is located, and R_0 the mean radius of the drop. Three points can be observed from this equation. First, when θ is zero, i.e., a wire has uniform cross-section, the corresponding capillary force is zero. Accordingly, a liquid drop does not move on this wire. Thus, a conical shape is needed. Second, the capillary force increases with the decrease in the wire radius and the increase in the apex angle, implying that thin wires with large variations in cross-sections are preferred in water

collection. Third, the capillary force also increases with the decrease in the drop volume, which means that a small drop moves faster than a large drop on a conical wire. All these three points have been validated in the above tests on the cacti (Figs. 2.1(b) and 2.1(c)) as well as in the previously reported tests [3].

2.3 Fabrication

2.3.1. Fabrication procedure

Branched ZnO nanowire structures have been recently synthesized using, for example, vapor-phase [31-34], solution-synthesis [35,36] or their combinations [37]. Their large surface areas make them have potential applications in, for example, solar energy conversion [37,38]. The concern here is how to make much larger branched structures.

There is a critical difference between the approaches of vapor phase and solution synthesis: the temperature used in a vapor-phase method normally ranges between 600 and 1000 ^{o}C [31-34], while the one adopted in solution synthesis method usually varies between 80 and 100 ^{o}C [35,36]. Due to this large difference in growth temperature (accordingly, there is a large difference in growth energy), during the same time period, wires grown using the vapor-phase approach are much longer (the lengths of the longest wires were reported to be 300 μm) [29] than the counterparts grown using the solution synthesis (the longest wires had the lengths of 40 μm) [39]. Thus, a vapor-phase approach is applied in our case to produce long stem and branched wires.

Vapor-solid (VS) [31,32] and vapor-liquid-solid (VLS) [33,34] are two commonly applied vapor-phase methods. The VS method is adopted here to grow wires, since we have rich experience with this approach. In the VS method, the substrate is coated with a layer of ZnO. The Zn and O_2 atoms are directly adsorbed on the surface of this ZnO seed layer, forming nuclei. ZnO wires grow out vertically from the nuclei in c-axis orientation.

The synthesis of branched ZnO wire structures involves two basic steps (Fig. 2.3). In the first step, stem wires are selectively grown on the ZnO film-covered sidewall of a Si substrate using a VS method [31,32] (Fig. 2.3(a)). In the second step, using the VS approach again, branched wires are synthesized on the ZnO film-covered sidewall of each stem wire, completing the fabrication of a branched structure (Fig. 2.3(b)). Three types of experiments are conducted. The first type of experiment is to grow ZnO stem wires, which corresponds to the first fabrication step. The second type is to examine the possibility of synthesizing relatively long wires on the sidewall of a long wire, and the third is to grow branched wires on the stem wires, which corresponds to the second fabrication step.
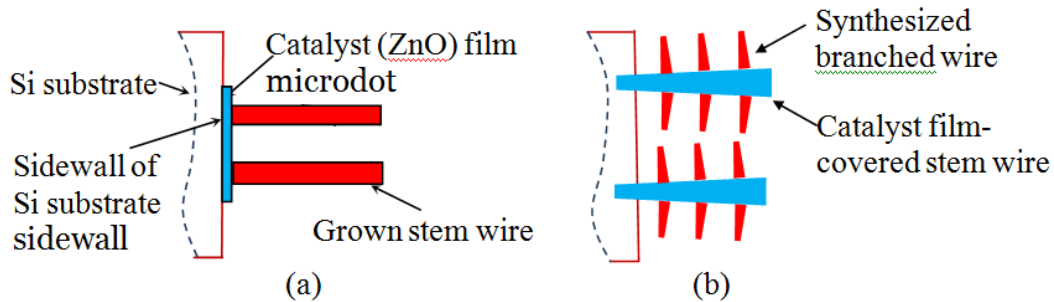
Figure 2.3 Procedure to fabricate branched ZnO wire structures: (a) Grow stem wires on the catalyst (ZnO) film located on the sidewall of a Si substrate, and (b) further synthesize branched wires on the catalyst film-covered sidewall of each stem wire.

2.3.2. Synthesis of stem wires

Fig. 2.4(a) shows a setup used in the first type of experiments. It includes a horizontal tube furnace and a quartz boat. ZnO and graphite powders are mixed on the surface of the quartz boat, which is subsequently placed in the center of the furnace. A Si substrate is placed on the quartz boat. After the tube in the furnace is heated up from room temperature to 950 °C, Ar and O_2 gases are introduced into the reactor. Meanwhile, Zn vapor is continuously generated by carbothermal reduction of ZnO powder in the

graphite crucible, following the chemical reaction: $C(s)+ZnO(s) \rightarrow CO(g)+Zn(g)$. The produced Zn vapor is brought over by the incoming gas flow to the Si substrate, and has reaction with O_2 over there to produce ZnO wires. After the high temperature is maintained for 20 h, Ar and O_2 systems are switched off and the furnace is cooled naturally to room temperature. The incoming Ar and O_2 flow have horizontal speeds of 85 and 2 sccm, respectively, while their vertical speeds are both zero.

The quartz boat consists of a horizontal plate and a movable vertical support. The horizontal plate has a small step on its back side. The substrate is put between this step and the vertical support. By moving the vertical support forward or backward along the horizontal plate, the substrate can be tilted at different angles. Consequently, the orientation of this substrate can be adjusted between 0° and 90° relative to the incoming gas flow.

Other researchers usually set the tilt angle to be 0° when growing ZnO structures [29,31-35,40]. However, in the first type of experiments, we changed the tilt angle to be 30° (Fig. 2.4(a)), resulting in a clear difference in the products generated on the edges and top surface of a Si substrate. An "edge effect" was found on the synthesized product. As shown in Fig. 2.4(b1), the lengths of ZnO wires were 484 μm on the top surface of the Si substrate, while ZnO wires grown on the edges of this substrate had the lengths of 4 to 5.5 mm, which are about 10 times longer than the ones on the top surface. The average diameters of the grown wires were 1 μm (Fig. 2.4(b2)). The selected-area electron diffraction (SAED) pattern of a 4-mm-long wire (the inset of Fig. 2.4(b3)), together with the top view of a representative ZnO wire (the insert of Fig. 2.4(b2)), shows that the ZnO wire has a hexagonal wurtzite structure with the growth direction along the direction of [0001] (i.e., c-axis). The first type of experiments indicates that, using our setup, it is feasible to generate mm-long stem wires on the sidewall of a Si substrate.

The "edge effect" is interpreted as follows. When a substrate experiences a gas flow, a relatively stagnant layer (i.e., a boundary layer) is formed on the surface of this substrate. The gaseous reactants have to diffuse through this boundary layer in order to reach the surface of the substrate to form the wires, and the concentrations of the gaseous reactants on this surface increase with the decrease in the thickness of this boundary layer [41]. According to Prandtl's boundary-layer theory [42], the boundary layer at the substrate edge is much thinner than that in the middle of the substrate, resulting in higher gas concentrations at the edges. In other words, during the same time period, the substrate edge experiences more gaseous reactants than the middle of the substrate. Thus, the ZnO wires grown on the edges were much longer than those at the center of the substrate in the first type of experiments.
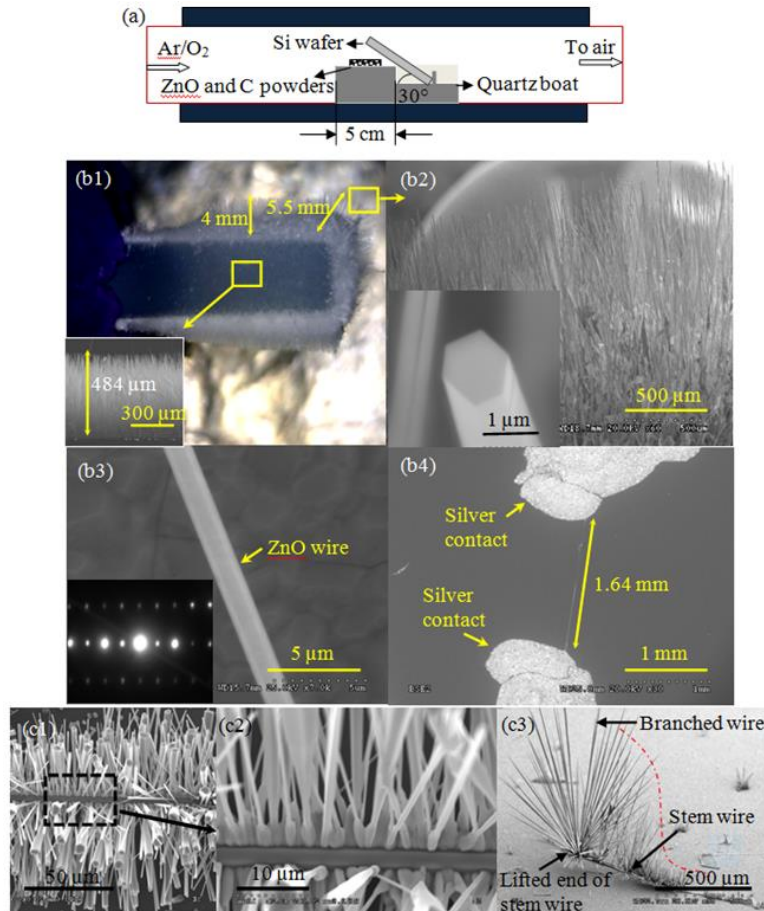
Figure 2.4 (a) Side view of a setup employed in the first two types of experiments to synthesize ZnO wires. (b1) Optical image of ZnO wires grown using this setup: wires with lengths of 484 μm were grown on the top surface, while wires with lengths of 4 to 5.5 mm were synthesized on the side edges of a silicon substrate (insert: side view of the 484-μm-long wires); (b2) close-up (SEM) view of the 5.5-mm-long ZnO wires (insert: perspective view of the top of a ZnO wire, indicating that it has hexagonal cross-sections); (b3) side (SEM) view of a ZnO wire (insert: the corresponding SAED pattern); and (b4) top (SEM) view of a 1.64-mm-long wire connected to two Ag pads at its ends. Branched wires generated on (c1) and (c2) a 4-mm-long flat wire, and on (c3) a partially lifted wire.

2.3.3. Growth of branched wires

Another experimental setup was adopted in the second and third types of experiments. It is similar to the one used in the first type of experiments, except for two critical differences (Figs. 2.4(a) and 2.5(a)): (i) a flowerpot-like crucible, which had a top opening with the diameter of 2 cm, was applied to contain ZnO and graphite powders; and (ii) the Si substrate was directly placed on the top opening of the crucible. Both changes were made to ensure that the ZnO wires were directly exposed in the incoming flow of Zn vapors.
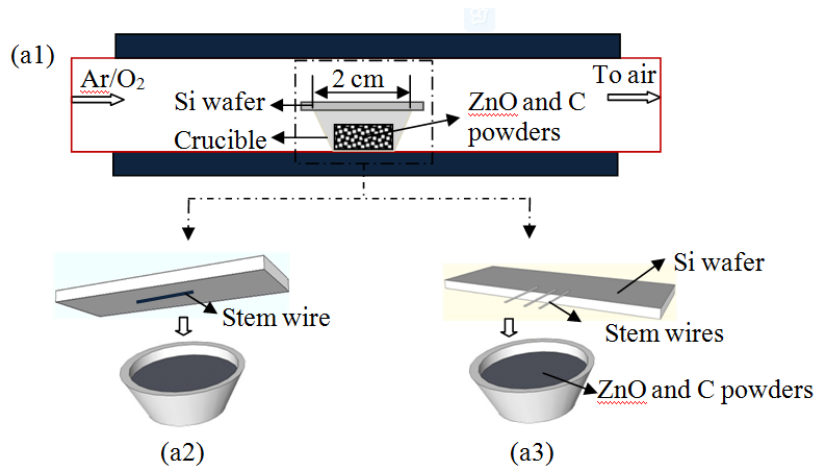
Figure 2.5 (a1) Side view of the setup for (a2) the second and (a3) third types of experiments.

In the second type of experiments, we examined whether long branched wires could be grown on the sidewall of a single wire to form a branched structure. The stem wires that were synthesized on the substrate edges in the first type of experiments were first manually placed on the center of a Si wafer (Fig. 2.5(a2)). The ZnO wires have an inherent charge. Accordingly, after a ZnO stem wire was put on the Si wafer, the electrostatic interactions [43] between them directly fixed the wire on the Si wafer. This Si wafer was subsequently flipped down on the crucible. The second type of experiments

includes two tests. In the first test, branched wires with lengths of about 30 µm were synthesized on the sidewalls of a 4-mm-long flat wire (Figs. 2.4(c1) and 2.4(c2)). Furthermore, in the second test, one end of a flat wire was lifted up before the growth of branched wires. As shown in Fig. 2.4(c3), branched wires with the lengths as long as 800 µm were grown on the lifted end of this wire (which was about 27 times as long as the ones generated in the previous test), and the lengths of the branched wires decreased from the lifted end towards the middle point of the flat wire, indicating that the "edge effect" can also be used to generate long branched wires. Based on the understanding gained from the first two types of experiments, branched wires were further grown on the stem wires in the third type of experiments. Part of a stem wire was put on the top surface of a Si substrate, while the remaining portion remained open to ensure that this portion was directly exposed to both Zn vapors and O_2 gases (Fig. 2.5(a3)).

Fig. 2.6(a) gives three representative branched wire structures synthesized out of the third type of experiments. Both stem and branch have conical shapes with apex angles of about 2° and 15°, respectively. The stem wire has a length ranging from 0.8 to 3.4 mm, and the diameter of its middle cross-section is about 25 µm. A branched wire has a length in the range of 20 to 400 µm, and the diameter of its middle cross-section is around 10 µm. These parameters are approximately in the same order as those of a branched wire structure on a cactus surface, while some branched wires are 7 times longer than their cactus counterparts (Fig. 2.1(a6)).
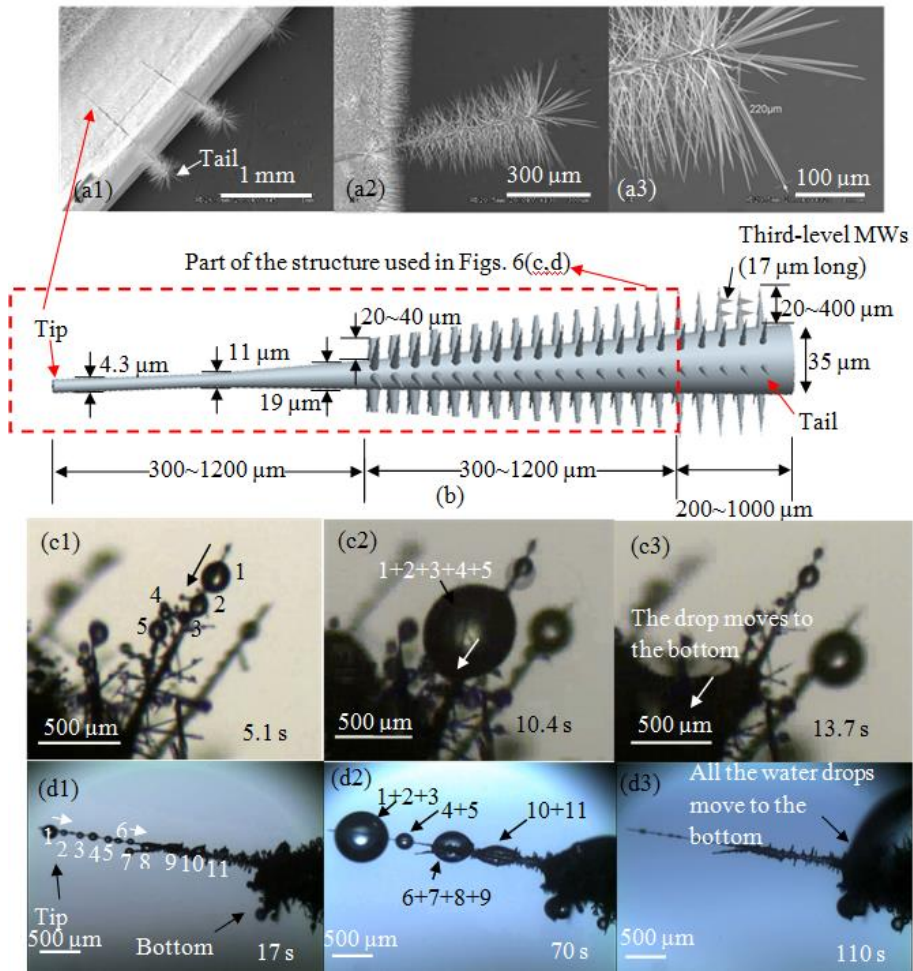
Figure 2.6 Synthesized branched wire structures: (a1) perspective view of three structures, (a2) close-up view of one of three structures, and (a3) magnified view of its tail portion. (b) Schematic of a synthesized structure. (c,d) Transportation and mergence of water drops on a synthesized branched wire structure: (c1) due to condensation of vapors, water drops appear on a branched wire, (c2) some drops merge into a large water drop in the middle of the branched wire, and (c3) the large drop further moves to the root of this wire. Transportation and mergence of large drops on the stem wire: (d1) water drops appear on the stem wire, (d2) these drops merge together to form several large drops, and (d3) the large drops move to the root of this stem wire.

All the wires in the synthesized structures have conical shapes. Due to "edge effect", the reactant concentration at a point of the stem wire gradually increases with the increase in the distance between this point and the substrate sidewall, resulting in two consequences. First, as observed in the second test of the second type of experiments, branched wires grown towards the open end of a suspended wire are longer than those close to the fixed end of this wire (Fig. 2.4(c3)). Second, the suspended wire gradually became thicker from the fixed end to the open one, forming a conical shape (Fig. 2.6(b)). On the other hand, the thickness of this wire increases at a lower rate than the length of a branched wire, since the sidewall growth of the wire is not along the preferred direction.

The formation of a conical branched wire is caused by two factors. First, a new portion of a wire is formed on the top surface of an existing part, and the cross-section of the new portion cannot be larger than that of the existing part. Second, Zn vapor concentration gradually decreases during the process of fabricating the branched wires, resulting in the decrease in chemical reaction rate. Accordingly, as previously reported [44], the new portions of branched wires have smaller cross-sections than the existing parts, forming conical shapes. The gradual reduction of Zn concentration is interpreted as follows. As observed from Figs. 2.5(a1) and (a3), O_2 gas has chemical reaction with Zn vapor at the top opening of the crucible to form branched wires. In addition, this reaction also occurs inside the crucible, which creates a thin ZnO film on top of the source materials (the film can be visibly seen after the fabrication is finished). This film gradually increases its area during the synthesis process, covering more source materials. Accordingly, the amount of Zn vapor that comes from the uncovered portion of the source material is gradually decreased, resulting in a lower Zn concentration around branched wires. However, this is not the case during the process of synthesizing stem wires in the first fabrication step. Due to "edge effect" and the driving effect of Ar flow, a less amount

of O_2 stays on the surface of source materials (Fig. 2.4(a)). Consequently, the created thin ZnO film just covers a small portion of the source materials. In addition, the surface area of the source materials is about 4.5 times as large as that in the process of fabricating branched wires. Thus, enough Zn vapor has been produced during the process of generating stem wires, making these wires have relatively uniform cross-sections.

2.4 Water-collection tests on artificial structures

2.4.1. Water-collection process

The synthesized branched wire structures were subsequently examined for their capability of collecting water using a setup the same as the one shown in Fig. 2.2. As marked in Fig. 2.6(b), the major part of a structure was used in such a test. After it was flipped, the corresponding tail portion was manually fixed on the tip of a needle using super-glue (Henkel Co., CT, USA), while the rest part remained open to incoming water vapors. Figures 2.6(c) and 2.6(d) give some testing results. The movements of condensed water vapors on both branched (Fig. 2.6(c)) and stem (Fig. 2.6(d)) wires are similar to what was observed on a cactus branched wire structure (Figs. 2.1(b) and 2.1(c)), and also match what was illustrated in Fig. 2.1(d). Within 110 s, all the drops that were specifically observed moved to the root of the tested structure (Fig. 2.6(d3)).

We noted that a water drop could still be collected even if a branched wire was oriented along the vertical direction with its tip located at the lower position, implying that all the wires in a structure have the capability of collecting water no matter what their orientations are. This phenomenon is interpreted using a theoretical result derived previously [6]. Let β denote the maximum tilt angle of the wire that water drop moves upwards along the wire (Fig. 2.7). Then, $-90^\circ \leq \beta \leq 90^\circ$, and we have [6]

$$\sin\beta = \frac{\theta l^2}{(r + \sqrt[3]{3V/4\pi})^2} \, , \qquad\qquad (2.2)$$

where l represents capillary length of water and equals 2.7 mm, and V is the drop volume. Three points can be observed from this equation. First, for a given water drop, β increases with the increase in θ and decrease in r. Second, if a wire has uniform cross-sections, which corresponds to the case that $\theta = 0^o$, then $\beta = 0^o$. This result implies that water could not move along the wire no matter how this wire is oriented, and that the wire should have varied cross-sections to make a water drop move. Third, when $\beta = 90^o$, which is the maximum tilt angle that a wire could have, in order to make water drops move upwards, by Eq. (2.2) the volume of a water drop should meet the following relation

$$V \le \frac{4\pi}{3}(l\sqrt{\theta} - r)^3 \, . \qquad\qquad (2.3)$$

According to the values of θ (about 15°) and r (around 5 μm on average) for a branched wire, Eq. (2.3) indicates that, if the volume of a water drop is not larger than 0.01 ml, then it can move upwards along a branched wire. Based on the values of θ (about 2°) and r (around 12.5 μm on average) for a stem wire, Eq. (2.3) shows that, if the drop volume is not larger than 0.0005 ml, then it can move upwards along the stem wire even if $\beta = 90^o$. On the other hand, according to our tests, a water drop has already moved upwards to the root along a vertically oriented branched wire when the drop volume is far below 0.0005 ml. As observed from Eq. (2.1), small water drops are easier to move than larger drops, since they suffer larger capillary forces. Hence, both stem and branched wires in the synthesized structure are capable of collecting water no matter how they are oriented.
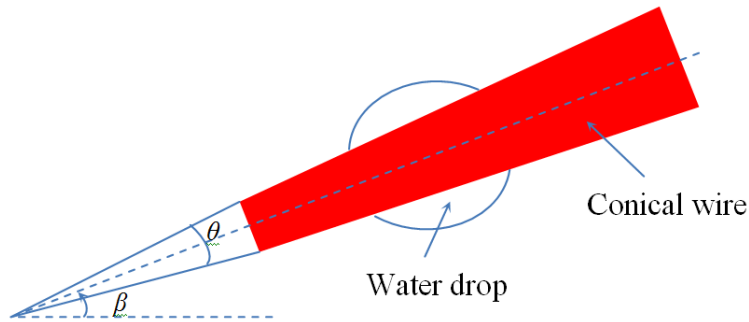
Figure 2.7 Geometric model of a water drop on a conical wire

2.4.2. Comparison of the water collection between artificial and cactus structures

Two groups of tests were done to compare water-collection efficiency of three artificial structures with another three cactus spines when the incoming mist flows had different directions (Fig. 2.8(a)). The mist flow direction was parallel to the longitudinal direction of a branched wire structure in the first group of tests, while it was perpendicular in the second group. In either group of tests, the artificial and cactus structures were each tested for five times. The stem wires in the three artificial structures, which are labeled as A1, A2 and A3 in Fig. 2.8(a), have lengths of 0.5, 0.64 and 1.12 mm, respectively. The three cactus structures are called C1, C2 and C3, which have lengths of 1.32, 0.77 and 1.53 mm, separately. It took an artificial structure a shorter time than a cactus one to collect a large drop, which covered the whole artificial structure (Figs. 2.8(b1) and 2.8(c1)). After this had occurred, the continuous collection of water replied on the adsorption of water vapors to the large drop, instead of the transportation of condensed drops through the wires. Accordingly, the time duration that we chose to compare water collection in a group of tests was the shortest period that it took collected water to cover an artificial structure among all the tests in this group. In the second group of tests, the flow direction was approximately perpendicular to the longitudinal direction of the branched wires that were located on the top half sidewall of the stem wire, while smaller

20

amounts of branched wires were directly exposed to the mist flow in the first group of tests. Consequently, the collecting duration of interest in the second group of tests was found to be 2 s (Fig. 2.8(c1)). It was much shorter than the one in the first group tests, which was 35 s (Fig. 2.8(b1)).
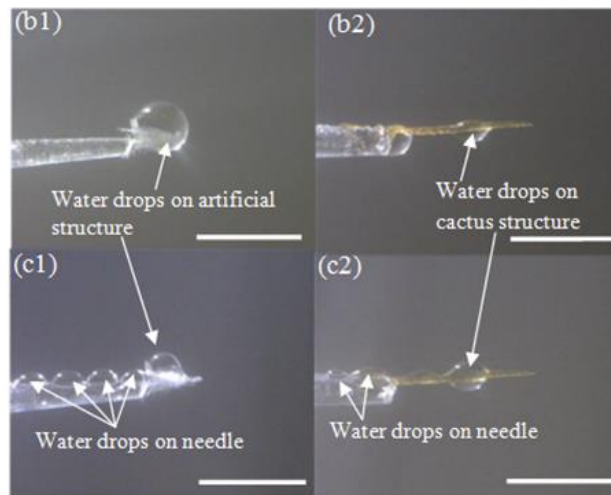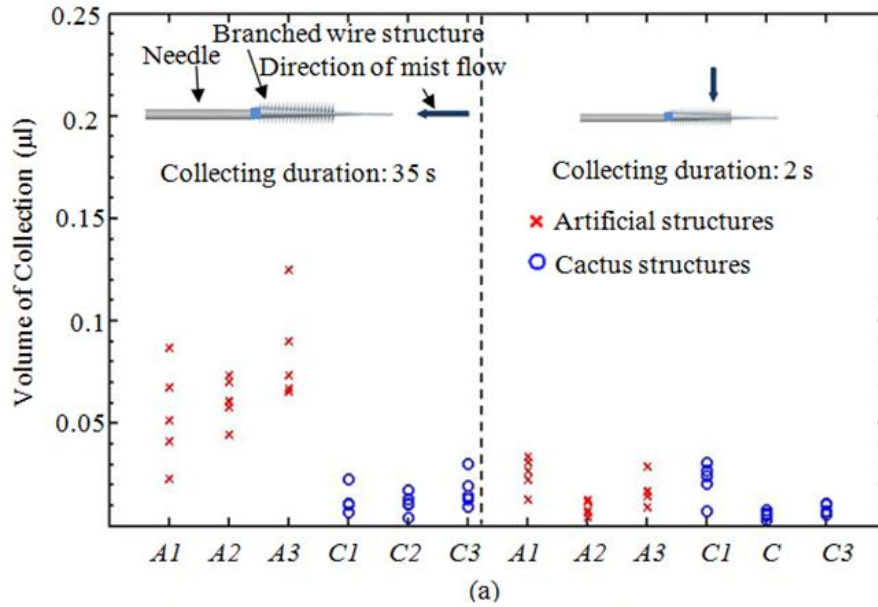
Figure 2.8 (a) Comparison of collected water between artificial and cactus branched wire structures. *A1-A3* and *C1-C3* denote artificial and cactus structures, respectively. Water drops collected by (b1) artificial (*A1*) and (b2) cactus (*C1*) structures in the first group of tests at the time instant of 35 s. Water drops collected by (c1) artificial (*A1*) and (c2) cactus (*C1*) structures in the second group of tests at 2 s. The scale bars represent 1 mm.

In the first group of tests, the amount of water collected by the artificial structure had a volume varying from 0.023 to 0.125 μl, which was calculated based on the measured diameter of a collected drop, and such a volume ranged from 0.004 to 0.03 μl in the case of the cactus structure. The average volumes collected by the artificial and cactus structures were 0.067 and 0.013 μl, respectively. This 5-time difference indicates that the artificial structure, in comparison with the cactus one, is more efficient in collecting water due to larger surface areas of its branched wires (some branched wires are 8.0 times as long as those of a cactus, and they are also more densely distributed on the stem wire). The comparison shows the importance of having ultra-long stem and long branched wires, which increase the surface areas of the structure for adsorbing more water vapors.

In the second group of tests, the volume of water collected by the artificial structure varied from 0.004 to 0.034 μl, while it ranged from 0.003 to 0.031 μl in the case of the cactus structure. The average volume collected by the artificial structure was 0.017 μl. It was about 1.4 times as large as that harvested by the cactus one, which was 0.012 μl. In this group of tests, water vapors were condensed on the whole surface of a structure, and they also quickly penetrated into the gaps between branched wires. Hence, water was not mainly collected by the movement of the drops on the wires. This point can also be observed from Figs. 2.8(c1) and 2.8(c2). Water drops were formed on needle surfaces as well, and had comparable sizes with those formed on the artificial or cactus structures, even if these surfaces were not covered by branched wires. In contrast, such phenomena were not observed in the first group of tests (Figs. 2.8(b1) and 2.8(b2)), indicating that branched wires play an important role in collecting water when a structure is not directly exposed to the mist flow.

2.4.3. Continuous collection of water by an artificial structure

        To explore the possibility of collecting water continuously by the as-grown branched wire structures, we first examined that mechanism that a cactus employed to absorb collected water drops from its branched structures into their underneath cluster. The test was on a dried cluster, whose cross-sectional view is given in Fig. 2.9. The inner structure of the cluster, which is marked as "Area A" in Fig. 2.9(a), is an array of hair-like trichomes [45]. These dried trichomes have relatively flat shapes (Fig. 2.9(b2)), probably due to loss of water. They have an average width of about 50 μm, and their lengths range from 0.3 to 3 mm. Underneath the cluster is thin-walled parenchyma [46], which is labeled as "Area B" in Fig. 2.9(a). Parenchyma is a water-storing tissue, and has a porous structure (Fig. 2.9(c)). As a drop of water was manually placed on a dried cluster, through capillary action, water gradually flowed into a large portion of the parenchyma via the gaps between the trichomes within 38 min (Fig. 2.10). As indicated in reference 47, the trichomes served as pathways during this water-absorption process. It is expected that, when the cactus is alive, the corresponding rate of water absorption may be much higher, since a water pressure difference can be created between the parenchyma and the cluster surface. This difference is induced by the loss of water inside the cactus, which may be caused by either (i) the transpiration [47] from the cactus surface, or (ii) the photosynthesis inside the cactus [48].
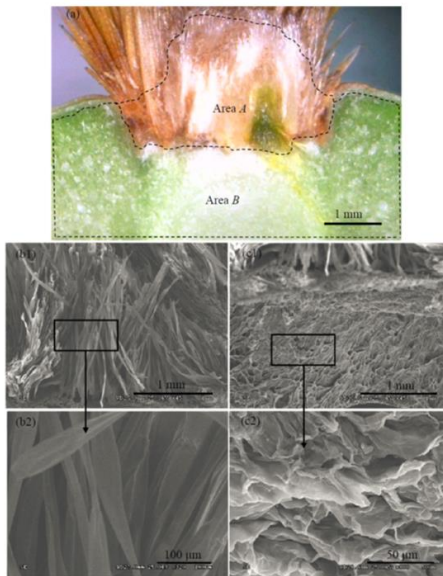
Figure 2.9 (a) Cross-sectional (digital) image of a cluster on the cactus *Opuntia engelmannii* var. *lindheimeri*. Close-up (SEM) views of Areas (b) *A* and (c) *B*.
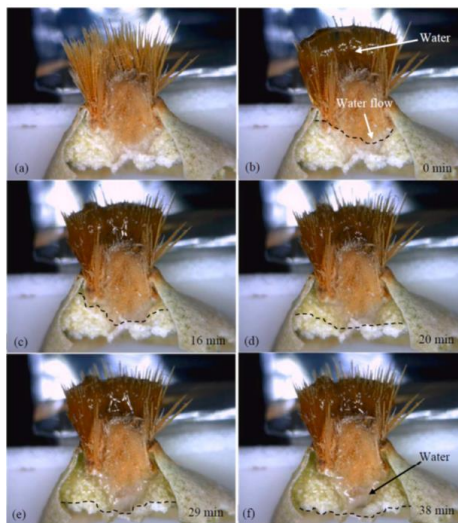
Figure 2.10 In-situ observation of the process that water was absorbed into a dried cactus cluster from its surface: (a) before and (b) after a large water drop was put on the cluster, and (c)-(f) water slowly moved inside the cluster. The dashed lines in (b-f) represent the fronts of water flow.

Based on the observed process of water absorption inside a dried cactus cluster, we then made three changes to the previous experimental setup (Fig. 2.2) to continuously collect water through an artificial structure (Fig. 2.11a): (i) a needle was located inside a glass tube with an inner diameter of 1.4 mm, (ii) a branched wire structure was positioned at the end of the glass tube that faced incoming mist flow, and (iii) a syringe was connected to the other end of the glass tube. The glass tube was applied to play the roles of both trichomes and parenchyma: guide a water flow, and store water. The syringe was used to create a pressure gradient for driving the collected water drops into the glass tube.

The mist flow direction was parallel to the longitudinal direction of a branched wire structure. A typical cycle of water collection includes three steps. First, water was first collected by the branched wires, and it then moved to the root of the structure (Figs. 2.11(a1) and 2.11(b1)). Second, the collected water was sucked into the glass tube due to a capillary force, which was caused by the curvature difference between the portion of the water drop outside and inside the glass tube (Figs. 2.11(a2) and 2.11(b2)). Third, the syringe was employed to pump the sucked water from right to left side of the glass tube (Figs. 2.11(a3) and 2.11(b3)). Water was continuously collected for 30 min. 20 cycles occurred during this period, the time for each cycle varied from 60 to 100 s, and totally about 6 μl water was collected.
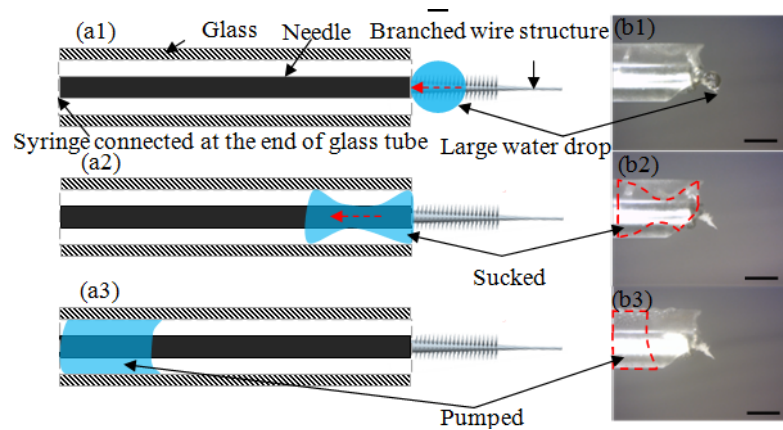
Figure 2.11 (a) Schematic and (b) experimental results of water collection process for one cycle. (a1, b1) A large drop is collected at the root of an artificial branched wire structure. (a2, b2) This large drop is sucked into glass tube by a capillary force. (a3, b3) The sucked water is pumped by the syringe from right to left, completing this cycle of collection. The scale bars represent 1 mm.

2.5 Summary and Conclusions

In this work, motivated by the water-collection approach of a cactus, we have developed an artificial branched wire structure to harvest water from fog and dew. An edge effect is employed to synthesize such a structure. As in the case of the cactus, all these wires in this structure have conical shapes, yielding a capillary force to drive a water drop to move from the tip of a wire to the root. On the other hand, due to relatively larger surface areas of the branched wires in the artificial structure, this structure collected more water in comparison with the cactus structure. In addition, it is also found that the amount of water collected is related to the direction of the incoming vapor flow. Finally, we have demonstrated that, with the aid of a syringe, large drops located at the root of a branched wire structure can be pumped into a glass tube, making this structure capable of continuously collecting water.

Chapter 3

Behavior of a liquid drop between two non-parallel plates

Liquid drops have shown interesting behaviors between two non-parallel plates. These plates may be fixed or movable relative to each other. In this work, we also explore these behaviors through a combination of theoretical and experimental investigations, and obtain some new results. We show that, when the two plates are fixed, different from the previous understanding, a lyophilic drop may not necessarily fill the corner of the two plates. We also demonstrate that it may fill the corner, when more liquid is added to the drop or when the top plate is lifted. Furthermore, we propose a physical model to interpret shifting effect of a liquid drop. This effect appears when the drop is squeezed and relaxed between two non-parallel plates, and it has been used by some shorebirds to transport prey. Based on the proposed model, we have found three new phenomena about the shifting effect.

3.1 Introduction

An angle inequality has been previously derived to judge whether a liquid drop fills the corner of two non-parallel plates [49,50]. This angle inequality was also obtained in one of our previous works during the process of exploring the condition for a liquid drop to fill microchannels [23]. According to the angle inequality, a lyophilic liquid drop, whose advancing contact angle on two plates is less than 90°, should first move towards and then fill the corner of these two plates, after it is put between them. The drop is propelled towards the corner due to a differential Laplace pressure along the length of the drop [51]. However, even if the angle inequality is satisfied, this self-propulsion may not always occur. For instance, as demonstrated by experiments in reference 51, a water drop did not fill a hydrophilic corner. In this work, we would like to explore the reason behind. In addition, it is worth mentioning that other researchers have also explored the spreading

behaviors of a liquid along the corner of two non-parallel plates [50,52-58], although these behaviors are not considered here. Angle inequalities are derived as well to judge whether a liquid drop has unbounded spread along the corner [50,53-56]. (see reference 50, for example, for a summary of these works).

In case a lyophilic drop is stationary between two non-parallel plates and does not fill their corner, such a lyophilic drop may be moved towards the corner by squeezing and relaxing the drop using these two plates [51,59]. As a matter of fact, some feeding shorebirds with long thin beaks, such as phalaropes, are currently using this approach to transport prey to their mouths [51,59-63]. If a lyophilic drop is pressed between two parallel plates, then, due to symmetry in geometry and pressure, the center of the drop does not change its position after squeezing and relaxing processes. Therefore, it is interesting to know why the whole drop translates when two non-parallel plates are used instead to press this drop. The corresponding physical mechanism responsible for the drop movement has been previously investigated by other researchers [51,59]. They indicated that contact angle hysteresis, together with wedge-like geometry, drives drops. Due to the wedge-like geometry, to maintain the pressure balance inside a static drop, contact angle at the leading edge of the drop is larger than the one at the trailing edge. When the squeezing and relaxing angles of the two non-parallel plates are optimized, the trailing and leading edges of the drop can be pinned, respectively, during the squeezing and relaxing processes. Accordingly, only the leading edge of the drop advances towards the plate corner during the squeezing process, while just the trailing edge has this movement during the relaxing process. The alternate movements of the two edges make the whole drop have one-directional translation towards the plate corner.

On the other hand, it is still not clear what has happened if both edges are not pinned. For instance, although contact angle at the trailing edge of the drop reaches

receding angle first, which makes this edge retreat first in the relaxing process, the leading edge may retreat faster, such that there may be no net drop motion in this process. To address such concerns, we also explore the corresponding physical mechanism in this work.

3.2 A liquid drop trapped between two fixed plates

In this section, we consider the behavior of a liquid drop that is located between two fixed plates. The bottom plate is oriented horizontally.

3.2.1. Preliminaries

As illustrated in Fig. 3.1, for simplicity, the left and right edges of the liquid drop are called "Edge 1" and "Edge 2," respectively, which are corresponding to the aforementioned leading and trailing edges. Use o and α, respectively, to denote apex edge and opening angle of the two plates. Let a_1 and b_1 denote the two points that Edge 1 intersects with the bottom and top plates, separately, and set a_2 and b_2 to be the two intersecting points that Edge 2 forms with the bottom and top plates, respectively. Use l_p to denote the distance between o and a_1, and let l_l be the length of $a_1 a_2$.

Set p_a and p_w to be atmospheric pressure and pressure inside the liquid drop, respectively. $(p_w - p_a)$ is so-called Laplace pressure. Let p_{w1} and p_{w2} represent liquid pressures at Edges 1 and 2, respectively.
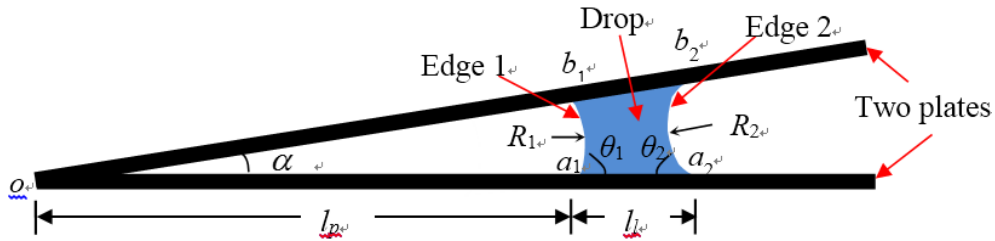
Figure 3.1 Cross-sectional schematic of a liquid drop placed between two non-parallel plates.

Two assumptions are made in this work. First, half heights of liquid drops are less than the capillary length of liquid, which is 2.7 mm in the case of water. Accordingly, the gravity effect on p_w is neglected, and p_{w1} and p_{w2} are uniform, respectively, on Edges 1 and 2 [23,64,65]. Subsequently, both Edges 1 and 2 are considered to be circular arcs [23]. Use R_1 and R_2 to represent the radii of these two edges, respectively. They are considered positive if their associated curves on the liquid surface bend towards air. Second, as done in previous works [23,51,59,64-66], the air/liquid interfaces between the two plates are considered to have approximately cylindrical, shapes. That is, a 2-D model is adopted to consider the wetting phenomena.

Let θ_1 represent equilibrium contact angle [67] at a_1 and b_1, and use θ_2 to stand for the one at a_2 and b_2. Based on the first assumption, it follows from geometric analysis that

$$\frac{1}{R_1} = \frac{-\cos(\frac{\alpha}{2} - \theta_1)}{l_p \sin\frac{\alpha}{2}}, \tag{3.1}$$

$$\frac{1}{R_2} = \frac{-\cos(\frac{\alpha}{2} + \theta_2)}{(l_p + l_l)\sin\frac{\alpha}{2}}. \tag{3.2}$$

Subsequently, in terms of both Young-Laplace equation [68] and the above two assumptions, p_{w1} and p_{w2} are, respectively,

$$p_{w1} = \frac{-\gamma\cos(\frac{\alpha}{2} - \theta_1)}{l_p \sin\frac{\alpha}{2}} + p_a, \tag{3.3}$$

31

$$p_{w2} = \frac{-\gamma \cos(\frac{\alpha}{2} + \theta_2)}{(l_p + l_l)\sin\frac{\alpha}{2}} + p_a,$$
(3.4)

where γ denotes the surface tension of the liquid, and $0^{\circ} < \alpha < \pi$.

Set θ_a and θ_r to be, respectively, advancing and receding angles. Then, both θ_1 and θ_2 vary between θ_r and θ_a. Since θ_r and θ_a are different on the surfaces of the plates used in this work, these surfaces are not ideally smooth, and may be marred by defects, such as chemical blemish or surface irregualarities [69]. A triple (air/solid/liquid) contact line is pinned on a plate surface until the corresponding contact angle increases to θ_a or decreases to θ_r. The cosine function is monotonically decreasing when its variable ranges from 0° to π. Accordingly, as observed from Eqs. (3.3) and (3.4), for fixed p_a, the increase or decrease of p_{w1} and p_{w2} implies the increase or decrease in θ_1 and θ_2. When p_{w1} is less than p_{w2}, to reduce the pressure difference, p_{w1} should increase, which results in the increase in θ_1, while p_{w2} should decrease, which causes θ_2 to decrease. If p_{w1} is still less than p_{w2} when θ_1 reaches θ_a, then Edge 1 advances towards the plate corner. Meanwhile, if θ_2 is decreased to θ_r, then Edge 2 retreats accordingly.

As given in the following four sub-sections, with the aid of Eqs. (3.3) and (3.4), the comparison of p_{w1} and p_{w2} results in four cases, whose results are subsequently validated by experiments.

3.2.2. Case I

If

$$\theta_a > (\frac{\pi}{2} + \frac{\alpha}{2}), \tag{3.5}$$

then the liquid drop cannot fill the corner of the two plates.

This claim is proved below. Assume that, even if Ineq. (3.5) holds true, the liquid drop still fills the corner. As Edge 1 approaches o during the process to fill this corner, we also have $l_p \to 0$ and $\theta_1 = \theta_a$. Subsequently, two points can be observed from Eq. (3.3). First, the denominator of the first term on the right-hand side of this equation approaches zero. Second, since Ineq. (3.5) is met, the numerator of the same term is positive. On the basis of these two points, it follows from Eq. (3.3) that $p_{w1} \to +\infty$. In contrast, l_l still has a finite value, and, by Eq. (3.4), p_{w2} also has a finite value for any allowed θ_2, which ranges from θ_r to θ_a. Therefore, $p_{w1} \gg p_{w2}$. This result implies that Edge 1 should either stop its movement or move away from the corner. Accordingly, the liquid drop cannot fill the corner, which is against our assumption that the liquid drop fills the corner. This contradiction means that our claim is true.

Ineq. (3.5) gives a sufficient condition for a liquid drop not to fill the corner of the two plates. The above proof also implies that, even if p_{w1} is initially lower than p_{w2}, which makes Edge 1 move towards o, there should exist a point close to o. At this point, Edge 1 stops its movement, since $p_{w1} = p_{w2}$. Ineq. (3.5) has been previously given, for example, in references 23, 49 and 50, and was also validated therein using numerical and experimental methods, respectively. Hence, experiments are not specifically conducted in this work to examine this inequality.

3.2.3. Case II

If

$$\theta_a < (\frac{\pi}{2} + \frac{\alpha}{2}) \,, \tag{3.6}$$

$$\alpha \ge (\theta_a - \theta_r) \,, \tag{3.7}$$

then the liquid drop fills the corner of the two plates.

This claim is proved below. Let $(p_{w1})_{max}$ represent the maximum value of p_{w1}, and set $(p_{w2})_{min}$ to be the minimum value of p_{w2} for fixed l_l and l_p. According to monotonically decreasing property of cosine functions, it follows from Eqs. (3.3) and (3.4) that: (i) $(p_{w1})_{max}$ is $[\dfrac{-\gamma \cos(\frac{\alpha}{2} - \theta_a)}{l_p \sin\frac{\alpha}{2}} + p_a]$, which occurs when θ_1 equals θ_a; and (ii)

$(p_{w2})_{min}$ is $[\dfrac{-\gamma \cos(\frac{\alpha}{2} + \theta_r)}{(l_p + l_l)\sin\frac{\alpha}{2}} + p_a]$, which happens if θ_2 is θ_r. When Ineq. (3.6) holds true,

$\cos(\frac{\alpha}{2} - \theta_a) > 0$. If Ineq. (3.7) is met, then $\cos(\theta_a - \frac{\alpha}{2}) > \cos(\frac{\alpha}{2} + \theta_r)$. Furthermore,

$\dfrac{1}{l_p} > \dfrac{1}{l_p + l_l}$. Hence, $(p_{w1})_{max} < (p_{w2})_{min}$. This result means that $p_{w1} < p_{w2}$ for any

allowed θ_1 and θ_2. Consequently, Edge 1 has to move towards o. In other words, due to the pressure difference, Edge 1 is pushed to move towards the corner until it reaches o. Subsequently, the liquid fills the corner. Thus, Ineqs. (3.6) and (3.7) form a sufficient condition for the filling to occur.

The result of this case is validated by two experiments, in which silicone oil and Isopropyl alcohol (IPA) drops were, respectively, tested. In the first experiment (Fig. 3.2), after a silicone oil drop had been placed between two SiO_2-coated Si plates, it kept moving towards the corner until it filled this corner. The same phenomena were observed

in the second experiment when an IPA drop was tested (figures are not shown). In the case of silicone oil, the values of α, θ_r and θ_a were measured to be 6°, 2°, and 3°, respectively, while for IPA these values were 6°, 14°, and 19°. Accordingly, both Ineqs. (3.6) and (3.7) are met. Thus, as predicated, either liquid drop filled the corresponding corner.
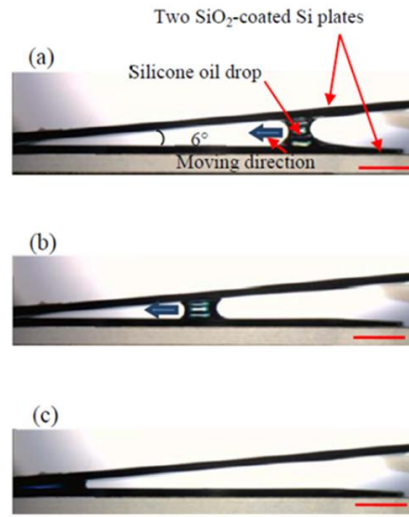
Figure 3.2 After a silicone oil drop had been placed between two SiO$_2$-coated Si plates, it (a,b) moved towards the corner formed by the two plates, and (c) finally filled this corner.

Scale bars represent 2.5 mm.

3.2.4. Case III

If both Ineq. (3.6) and the following inequality

$$\alpha < (\theta_a - \theta_r) \tag{3.8}$$

hold true, then the corner may not necessarily be filled. Since Ineq. (3.8), instead of Ineq. (3.7), is now satisfied, we have

$$\cos(\theta_a - \frac{\alpha}{2}) < \cos(\frac{\alpha}{2} + \theta_r), \tag{3.9}$$

35

instead of $\cos(\theta_a - \frac{\alpha}{2}) > \cos(\frac{\alpha}{2} + \theta_r)$. Therefore, the proof of Case II does not apply here.

The above claim is proved as follows. Let's consider two examples. In the first example, the drop size is much smaller than the distance between Edge 1 and o. That is, $l_p \gg l_l$. Subsequently, it follows from Eq. (3.4) that

$$ p_{w2} = \frac{-\gamma \cos(\frac{\alpha}{2} + \theta_2)}{l_p \sin \frac{\alpha}{2}} + p_a. \qquad (3.10) $$

In this example, in order to fill the corner, the whole drop should move towards o. Accordingly, $\theta_1 = \theta_a$ and $\theta_2 = \theta_r$. Subsequently, with the aid of Ineq. (3.9), it follows from Eqs. (3.3) and (3.10) that $p_{w1} > p_{w2}$, implying that Edge 1 should either stop its movement or move away from the corner. If Edge 1 keeps moving away from the corner such that $l_p \to +\infty$, then it follows from Eqs. (3.3) and (3.10) that $p_{w1} = p_{w2} = p_a$, indicating that the liquid drop should eventually be stationary. Consequently, the liquid drop considered in this example should be finally at rest, and does not fill the corner. In the second example, a liquid drop is placed very close to the corner such that $l_p \to 0$. Accordingly, by Eq. (3.3), $p_{w1} \to -\infty$. In contrast, l_l still has a finite value, and, by Eq. (3.4), p_{w2} has a finite value as well for any allowed θ_2, which ranges from θ_r to θ_a. Hence, $p_{w1} \ll p_{w2}$, indicating that Edge 1 is pushed towards the corner until it reaches o. These two examples indicate that, depending on the values of l_p, l_l, θ_1 and θ_2, a liquid drop may or may not fill the corner of the two plates.

In reference 51, after a water drop had been put between two stainless steel beaks, the drop was at rest (see its Fig. 3(A)). The corresponding values of θ_r and θ_a

36

were about 20° and 65°, respectively, and the value of α was less than 4.0°. p_{w1} and p_{w2} were not compared here due to lack of the values of l_p, l_l, θ_1 and θ_2. On the other hand, since Ineqs. (3.6) and (3.8) were both met, it was possible to have a stationary drop in this special situation.
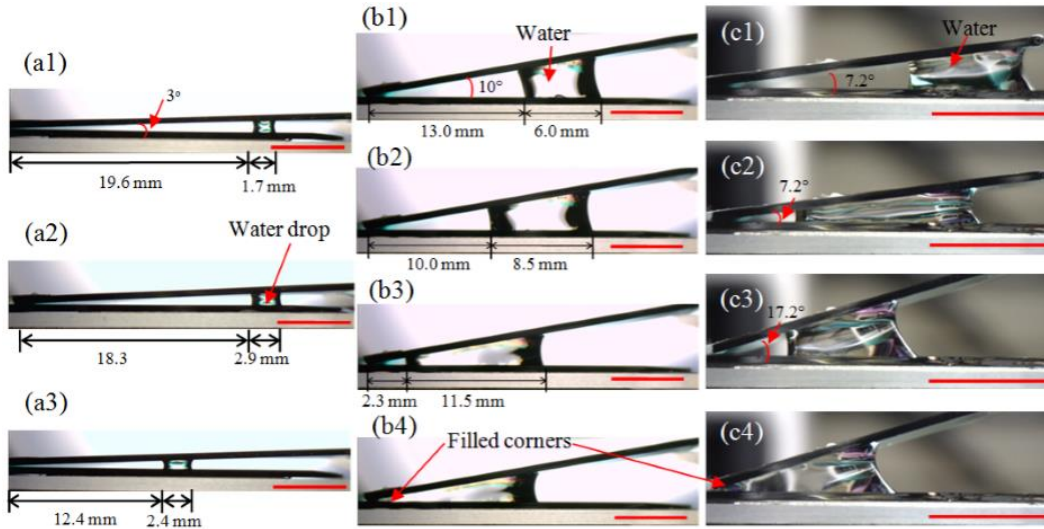
Figure 3.3 (a) Three examples that, when $l_p/l_l>5.1$, a water drop was at rest. (b1) A water drop was initially at rest; (b2) when water was added to increase l_l from 6.0 to 8.5 mm, (b3) the drop started to move towards the apex edge, and (b4) finally filled the corner. (c1) A water drop was initially at rest; (c2) after water was added to increase l_l, the drop moved and stopped a location close to the apex edge; (c3) when the top plate was lifted up to increase α from 7.2° to 17.2°, the drop started to move again towards the apex edge, and (c4) finally filled the corner. Scale bars represent 6 mm.

Five points can be obtained from the two examples of the proof and the comparison of p_{w1} and p_{w2}.

If the drop size is much smaller than the distance between Edge 1 and o, i.e., $l_p \gg l_l$, then the drop is at rest, which is the result of the first example.

37

If $I_p << I_l$, which is true when Edge 1 is close to o or when the drop size is large, then $p_{w1} << p_{w2}$. Subsequently, Edge 1 should move towards o till the corner is filled. This point can be readily proved, using a line of reasoning similar to the one adopted in the second example.

Given that we initially have $p_{w1} = p_{w2}$, if we keep adding the liquid to the drop to make I_l much larger than I_p, which is the case of the second point, then Edge 1 should move towards o till the corner is filled. This gives an approach to make a drop, which is initially at rest, fill the corner if the addition of the liquid is allowed.

Given that we initially have $p_{w1} = p_{w2}$, if we lift the top plate to increase α to a value such that Ineq. (3.8) is violated while Ineq. (3.7) holds true, then according to the result of Case II, Edge 1 should move towards o till the corner is filled. This gives another approach to make a stationary drop fill the corner.

If we initially have $p_{w1} > p_{w2}$, then Edge 2 should move away from the corner while it should stop somewhere. As observed from the first point, the drop should at least stop when the condition that $I_p >> I_l$ is met. That is, a drop between the two plates cannot keep moving away from the corner by itself.

Four types of experiments were done to validate the first four points, respectively, and water drops and SiO$_2$-coated Si plates were used in all these experiments. The corresponding values of θ_r and θ_a were measured to be 50°, and 67°, separately. Except for the fourth type of experiments, in which Ineq. (3.8) might not be satisfied while Ineq. (3.6) still held true, these two Inequalities were met in all other experiments. In the first type of experiments, when I_l was more than five times as large as I_p, a water drop was found to be stationary (Fig. 3.3a). In the second type of experiments (figures are not

shown), when l_l and l_p were larger than 10 mm and less than 2 mm, respectively, a water drop always filled the corner after the placement. In the third type of experiments, water was added to a stationary drop. Due to this addition, l_l was increased, while l_p was reduced to achieve new balance between p_{w1} and p_{w2}. As shown in Fig. 3.3(b), when l_l was increased from 6.0 to 8.5 mm and l_p was reduced from 13.0 to 10.0 mm, the drop started to move towards o until it finally filled the corner. In the fourth type of experiments, as shown in Figs. 3.3(c1) and (c2), a stationary drop first moved towards o after addition of water, and then stopped. Subsequently, when α was increased from 7.2° to 17.2°, which resulted in the violation of Ineq. (3.8) but the satisfaction of Ineq. (3.7), the drop began to move again and eventually filled the corner as expected (Figs. 3.3(c3) and 3.3(c4)). In addition, in all the tests, we did not observe any drops that kept moving away from the corner, which validates the fifth point.

3.2.5. Case IV

If

$$\theta_a \leq \frac{\alpha}{2}, \tag{3.11}$$

then the corner should be filled. This inequality is a special case of Ineq. (3.6). Also, it is readily shown that, once Ineq. (3.11) is met, Ineq. (3.7) is also satisfied. Thus, according to the result of Case II, Ineq. (3.11) is also a sufficient condition for the filling to occur. The values of θ_a that meet Ineq. (3.11) form a sub-set of those which satisfy Ineqs. (3.6) and (3.7). Therefore, Case IV is actually a special one of Case II. Since it is simple to use Ineq. (3.11) to judge the filling of the corner, this special case is specifically listed here.

The two experiments of Case II were repeated. However, to make Ineq. (3.11) hold, the values of α were increased to 8° and 40°, respectively. As expected, the corresponding liquid drops also filled the corner in either test (Fig. 3.4).
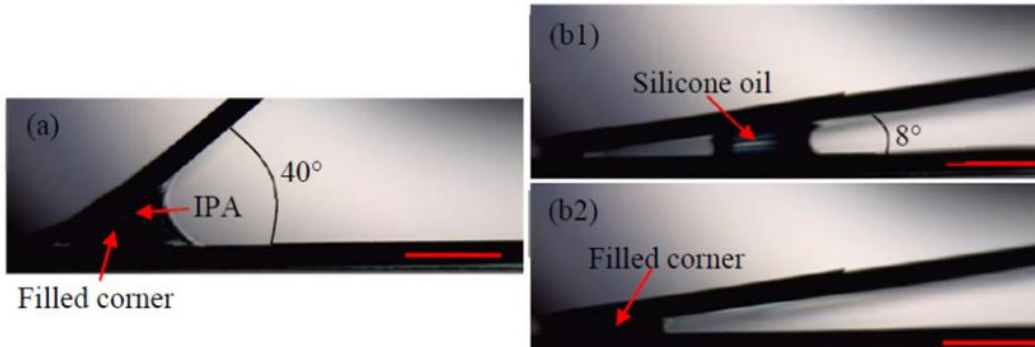
Figure 3.4 When the values of α were 40° and 8°, respectively, (a) IPA and (b) silicone

oil drops filled the corners. Scale bars represent 2 mm.

Cases I and II have been previously discussed in references 23 and 49. On the

other hand, the theoretical model of reference 49 did not consider contact angle

hysteresis. That is, in their model, it was assumed that $\theta_a = \theta_r$. Therefore, their model is

not accurate to predict the filling result in Case III, when there exists the contact angle

hysteresis. In the case of reference 23, it was assumed that Edge 2 always bent towards

air. Accordingly, $p_{w2} > 0$. Thus, the corresponding model is not accurate to predict the

filling condition in Case III, when Edge 2 of a lyophilic drop bends towards liquid. As just

demonstrated in Cases I through IV, this work does not have the aforementioned

assumptions, making the derived results have better prediction.

3.3 Squeezing and relaxing of a drop between two non-parallel plates

3.3.1. Model

A typical cycle of squeezing and relaxing a lyophilic drop is given in Fig. 3.5. In

the squeezing process (Figs. 3.5(a1), 3.5(a2), 3.5(b1) and 3.5(b2)), the lyophilic drop is

pressed by the top plate, and its Edges 1 and 2 move left- and rightwards, respectively,

resulting in a pancake-like shape. In the relaxing process (Figs. 3.5(a3), 3.5(a4), 3.5(b3)

and 3.5(b4)), the top plate is lifted up, Edge 1 slightly moves rightwards, while Edge 2

has a relatively large displacement along the opposite direction. As a result, the whole liquid drop is shifted towards *o*. Repetition of these two processes results in the continuous movement of the drop towards *o*. A water drop and two SiO_2-coated plates were used in the experiment shown in Fig. 3.5(a).
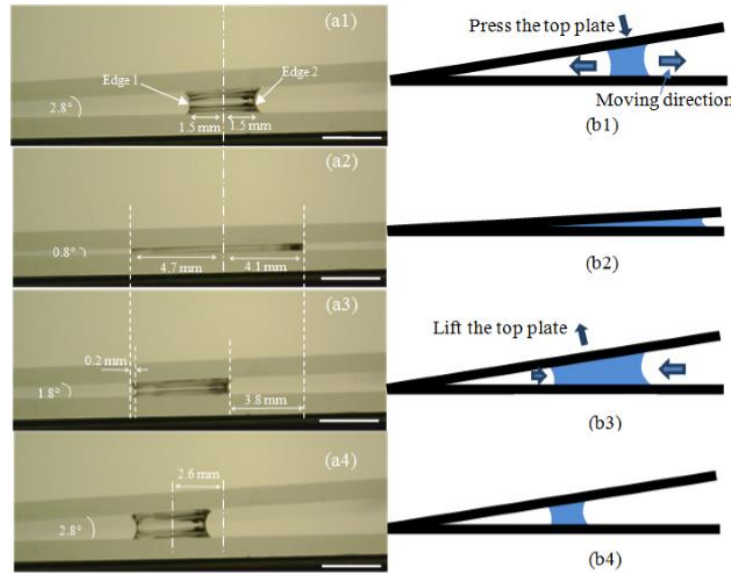
Figure 3.5 (a) Cross-sectional schematics and (b) experimental results of squeezing and relaxing a lyophilic liquid drop: (a1,b1) squeezing of the drop, (a2,b2) squeezed drop, (a3,b3) relaxing of the drop, and (a4,b4) relaxed drop. Scale bars represent 1 mm.

A physical model is proposed to explain the shifting effect of the squeezing and relaxing processes. When the liquid drop is pressed, the liquid pressure at b_1b_2, which is the interface between the drop top and the top plate, is increased. This pressure is now higher than those at Edge 1, Edge 2 and a_1a_2. Hence, as illustrated in Fig. 3.6(a), the liquid is driven by the pressure difference to flow towards these edges, making Edges 1 and 2 moving left- and rightwards, respectively.

When the liquid drop is relaxed by lifting the top plate, the liquid pressure at b_1b_2 is reduced. This pressure is now lower than those at Edge 1, Edge 2 and a_1a_2. As

illustrated in Fig. 3.6(b), the liquid is driven by the pressure difference to flow away from these edges, making Edges 1 and 2 moving right- and leftwards, respectively.
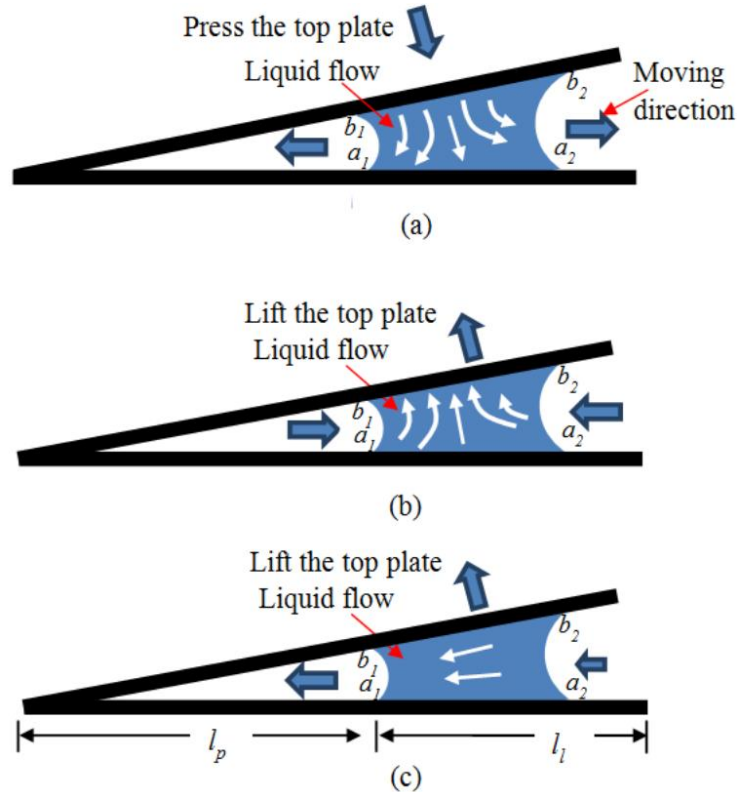
Figure 3.6 Cross-sectional schematics of flow patterns and edge movements of a lyophilic liquid drop during (a) squeezing and (b,c) relaxing processes.

To have shifting effect, at least the following two conditions should be met: (i) θ_1 equals θ_a during the squeezing process, and (ii) θ_2 is θ_r during the relaxing process, As observed from Eq. (3.3), if θ_a is large, then p_{w1} should be high in the squeezing process. Accordingly, the liquid drop should be pressed more to make Edge 1 progress outwards. That is, the opening angle of the two plates should be small to make Edge 1 advance. Conversely, if θ_r is small, then the opening angle of the two plates should be large in the relaxing process to make Edge 2 retreat inwards. In other words, the difference between

the values of α in the squeezing and relaxing process should be large when contact angle hysteresis is large, which has actually been experimentally demonstrated in reference 51. Meanwhile, during the squeezing and relaxing processes, due to the movements of Edges 1 and 2, the interface b_1b_2 also increases and decreases its size, respectively.

In terms of deformation and movement of the drop, it appears that the relaxing is a reversible process of the squeezing. However, as justified below, this is not necessarily true. In the relaxing process, when Edges 1 and 2 move towards each other, both θ_1 and θ_2 equal θ_r. At the end of the squeezing process, α is much smaller than θ_r, which also holds true at least at the beginning stage of the relaxing process. Subsequently, by Eqs. (3.3) and (3.4), the corresponding p_{w1} and p_{w2} can be approximated as:

$$p_{w1} = \frac{-\gamma \cos \theta_r}{l_p \sin \dfrac{\alpha}{2}} + p_a, \qquad (3\text{-}12)$$

$$p_{w2} = \frac{-\gamma \cos \theta_r}{(l_p + l_l) \sin \dfrac{\alpha}{2}} + p_a. \qquad (3\text{-}13)$$

It follows from these two equations that $p_{w1} < p_{w2}$. As shown in Fig. 3.6(c), the difference between these two pressures drives liquid to flow from Edges 2 to 1, making Edge 1 move leftwards. Accompanied with this flow, Edge 2 may also move leftwards. The combination of the two situations shown in Figs. 3.6(b) and 3.6(c) indicates that the rightward movement of Edge 1 is reduced or stopped, while the leftward movement of Edge 2 may be enhanced. Accordingly, the drop is shifted leftwards at the end of the relaxing process in comparison with the corresponding position at the beginning of the squeezing.

The critical difference between the squeezing and relaxing processes is that, in the squeezing process, even if there exists a difference between p_{w1} and p_{w2}, this difference does not cause a horizontal flow inside the drop, since the pressure in the middle of the drop, p_{wm}, is larger than both p_{w1} and p_{w2}. As illustrated in Fig. 3.6(a), ($p_{wm} - p_{w1}$) and ($p_{wm} - p_{w2}$) make liquid move left- and rightwards, respectively. However, in the relaxing process, p_{wm} is less than both p_{w1} and p_{w2}. Hence, in addition to the flow patterns illustrated in Fig. 3.6(b), liquid between Edges 1 and 2 can also be pushed to flow leftwards by ($p_{w2} - p_{w1}$) (Fig. 3.6(c)). Therefore, in terms of the movements of Edges 1 and 2, the relaxing is not a reversible process of the squeezing. On the other hand, if the two plates are parallel, i.e., $\alpha = 0^{\circ}$, then, due to geometric symmetry, we have $p_{w2} = p_{w1}$. Accordingly, the flow pattern shown in Fig. 3.6(c) does not exist. Thus, the relaxing is a reversible process of the squeezing, and there is no shifting effect, as previously observed in experiments [30,64,70,71].

It has been shown in references 51 and 59 that, due to wedge-like geometry, θ_1 is larger than θ_2 in a static drop. Accordingly, it is considered that the translation of a drop is induced by two factors [51,59]: (i) Edge 1 progresses outwards first in the squeezing process, since θ_1 reaches θ_a before θ_2; and (ii) Edge 2 retreats inwards first in the relaxing process, because θ_2 reaches θ_r before θ_1. As discussed in Section 1, when Edges 1 and 2 are not pinned during a processing cycle, these two factors may not be sufficient enough to explain the shifting effect. The proposed model indicates that, in addition to these two factors, the difference between p_{w1} and p_{w2} during the relaxing process creates a horizontal flow from Edges 2 and 1. This flow reduces the retreating distance of Edge 1 but increases that of Edge 2, making the relaxing not a reversible

44

process of the squeezing. Hence, after a processing cycle, a lyophilic drop translates relative to the original position of the drop.

3.3.2. In-situ observation of the flows inside water drops

To validate the proposed model, as done in one of our previous works [72], the flows inside water drops were directly observed with the aid of microparticles when these drops are squeezed and relaxed. To clearly see the movements of microparticles, a lamp was placed beside the corresponding experimental setup to provide additional light. Since the previously used Si plates blocked light, glass slides, which were transparent to light, were used instead in this type of tests. The corresponding values of θ_r and θ_a were measured on the glass slides to be 30° and 69°, respectively. 0.2 g graphite particles with diameters in the range of 10 to 20 µm and mass density of 1,900 kg/m^3 (Sigma-Aldrich Corp.) were added into 20 ml de-ionized water, followed by stirring the solution for at least 5 min. 10 µl water drops were placed between two non-parallel glass slides. The flow directions were observed according to the moving directions of the microparticles during a processing cycle (Fig. 3.7(a)).
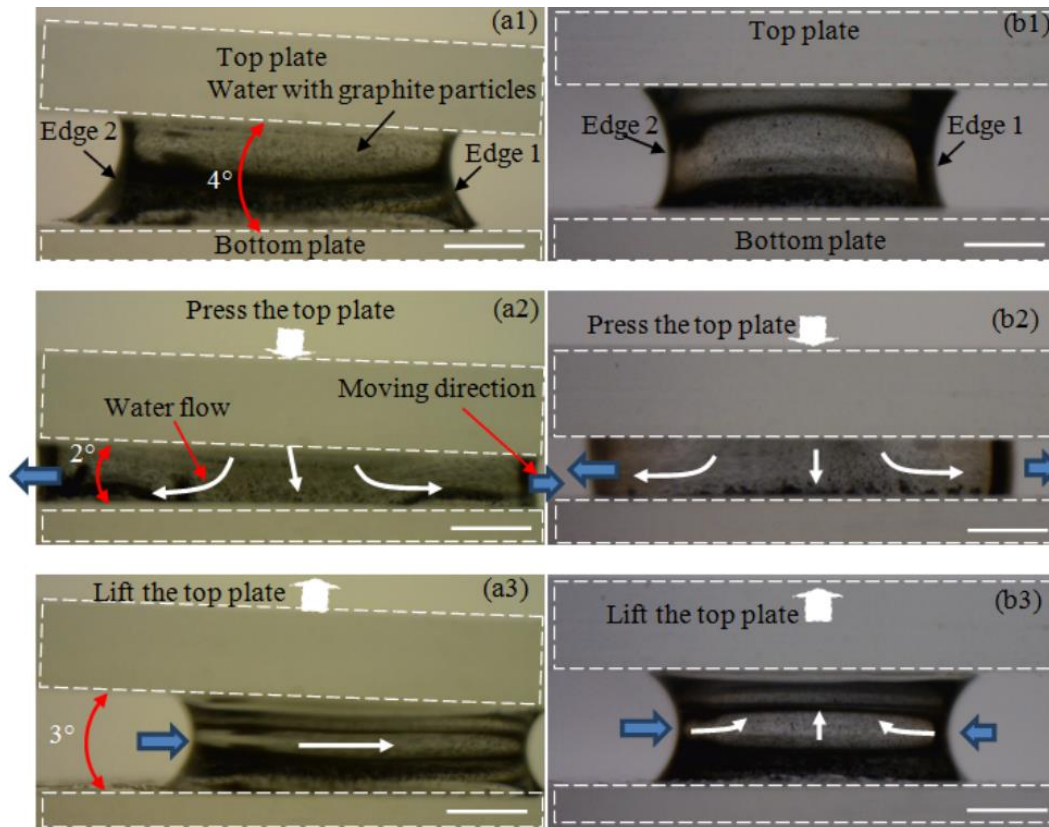
Figure 3.7 Observation of flow directions inside a water drop during the squeezing and relaxing processes with the aid of graphite microparticles (cross-sectional views). Case of two non-parallel plates: (a1) mix water with graphite particles and add a drop between two plates, (a2) squeeze and (a3) relax the drop. Edge 1 was found to be pinned during the relaxing process. Case of two parallel plates: (b1) mix water with graphite microparticles and add a drop between two plates, (b2) squeeze and (b3) relax the drop. Scale bars represent 1 mm.

For the purpose of comparison, the same tests were also done between two parallel glass slides (Fig. 3.7(b)). Since the two glass slides were not ideally parallel, the motions of Edges 2 and 1 were not symmetric with respect to the central line of the drop. Edge 2 actually progressed outwards and retreated inwards more than Edge 1 during the

squeezing and relaxing process. On the other hand, these two edges moved back to their original positions after a processing cycle (Fig. 3.7(b)).

In addition, three points are observed from Fig. 3.7. First, as seen from Fig. 3.7(a), the observed flow directions during the squeezing process in the case of the two non-parallel glass slides are similar to what has been illustrated in Fig. 3.6(a). Second, there exists a horizontal flow inside the water drop from Edges 2 to 1 in the relaxing process (Fig. 3.7(a3)), which validates the corresponding theoretical prediction (Fig. 3.6(c)). Third, as seen from Fig. 3.7(b), the flow pattern during the squeezing process in the case of the two parallel glass slides are similar to the counterpart in the case of the non-parallel glass slides, while the flow directions in the relaxing process are different from the corresponding counterparts but similar to what has been illustrated in Fig. 3.6(b). In summary, the in-situ observed flow directions match those predicted in the theoretical model.

3.3.3. Three new phenomena and experimental validation

Three new phenomena are further predicted using the proposed model. The first phenomenon is that, the closer a drop gets to *o* before a processing cycle, the longer distance this drop transports towards o after this cycle. According to Eqs. (3.12) and (3.13), we have

$$p_{w2} - p_{w1} = \frac{\gamma \cos \theta_r}{\sin \frac{\alpha}{2}} [\frac{1}{l_p} - \frac{1}{l_p + l_l}] . \qquad (3.14)$$

By this equation, it is readily shown that, for fixed α and l_l, ($p_{w2} - p_{w1}$) increases with the decrease in l_p. Accordingly, the leftward movements of both Edges 1 and 2 that are illustrated in Fig. 3.6(c) should also increase with the decrease in l_p.

The second phenomenon is that, in the case of a lyophobic drop, the drop should move away from o after a processing cycle. Although a lyophilic drop is considered in the

proposed model, this model can also be extended to the case of a lyophobic drop, whose θ_r is large than 90°. When a lyophilic drop is replaced by a lyophobic drop, the critical difference is that we will have $p_{w1} > p_{w2}$, which is derived using Eq. (3.14). Accordingly, the flow shown in Fig. 3.6(c) should be along the opposite direction. Thus, a lyophobic drop should move away from o after a processing cycle.

The third phenomenon is that the shifted distance of a lyophobic drop after a processing cycle decreases with the increase in the initial distance, which the drop has from o before the processing cycle. This phenomenon can be readily justified using a line of reasoning similar to the one used to predict the first phenomenon.

These three predicted phenomena are subsequently examined through two experiments. In the two experiments, SiO_2- and Teflon-coated Si plates were, respectively, used to manipulate water drops. As previously indicated, SiO_2-coated surfaces are hydrophilic. In contrast, Teflon-coated plates are hydrophobic, and the corresponding values of θ_r and θ_a were measured to be 114° and 129°, separately. In the first experiment (Fig. 3.8a), as expected from the first point of the model, the moving distance of the drop after a processing cycle increased when this drop gets closer to the corner. It moved about 3.0, 3.7 and 6.7 mm, respectively, after the first, second and third cycles. After one more cycle, the water drop filled the corner of the two plates. On the contrary, in the second experiment (Fig. 3.8b), a water drop was transporting away from the corner. This drop moved about 3.1, 2.0 and 1.6 mm, respectively, after the first, second and third cycles. After 15 cycles, the drop did not show any visible movement when it was further squeezed and relaxed. The results in the second experiment validate the second and third points derived from the proposed model.
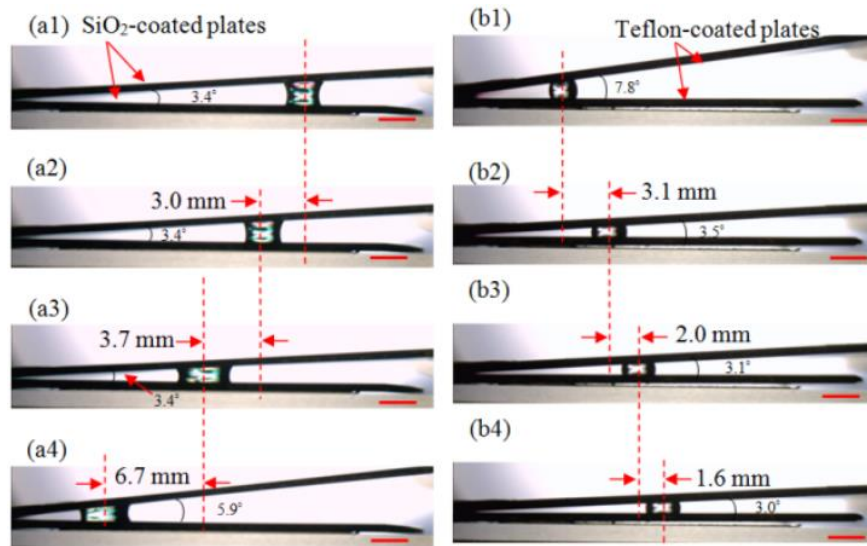
Figure 3.8 Three cycles of squeezing and relaxing processes of (a) lyophilic and (b) lyophobic drops. (a1, b1) a drop is placed between two plates. The results of (a2,b2) first, (a3,b3) second, and (a4,b4) third cycles. Scale bars represent 2.5 mm.

3.4 Summary and conclusions

In this work, through the comparison of the liquid pressures on two opposite edges of a liquid drop, together with the consideration of contact angle hysteresis, we have considered four possible cases, and identified whether a liquid drop fills the corner of two non-parallel plates in each case. We have also developed two approaches that may enable an initially stationary drop to fill the corner. Furthermore, we have proposed a model to interpret the shifting effect of a liquid drop when it is squeezed and relaxed between two non-parallel plates. Three new phenomena were predicted based on this model, which were subsequently validated by two experiments.

Chapter 4

Bio-inspired Plate-based Fog Collectors

In Chapter 3, we have explored the feeding mechanism of a shorebird to transport liquid drops by repeatedly opening and closing its beak. In this chapter, we apply the corresponding results to develop a new artificial fog collector. The collector includes two nonparallel plates. It has three advantages in comparison with existing artificial collectors: (i) easy fabrication, (ii) simple design to scale up, and (iii) active transport of condensed water drops. Two collectors have been built. A small one with dimensions of 4.2 x 2.1 x 0.05 cm^3 (length x width x thickness) was first built and tested to examine: (i) the time evolution of condensed drop sizes, and (ii) the collection processes and efficiencies on the glass, SiO_2, and SU-8 plates. Under similar experimental conditions, the amount of water collect per unit area on the small collector is about 9.0, 4.7 and 3.7 times, respectively, as much as the ones reported for beetles, grasses and metal wires, and total amount of water collected is around 33, 18 and 15 times. On the basis of the understanding gained from the tests on the small collector, a large collector with dimensions of 26 x 10 x 0.2 cm^3 was further built and tested, which was capable of collecting 15.8 mL water during a period of 36 min. The amount of water collected, when it is scaled from 36 to 120 min, is about 878, 479 or 405 times more than what was collected by individual beetles, grasses or metal wires.

4.1 Introduction

Various hierarchical wire structures, such as branched ZnO nanowire structures [31-37], have been recently synthesized. Their large surface areas make them have potential applications in, for instance, solar energy conversion [37,38]. However, the lengths of the structures are normally in the microscale, and the branched wires in the nanoscale. In contrast, the hierarchical wire structures of plants have at least mm-scaled

lengths. Accordingly, as discussed in Chapter 2, we have recently developed branched ZnO wire structures, whose sizes are comparable to or larger than the spine structures of the cacti [73]. They have been successfully applied to collect water. In addition, other researchers also reported continuous collection of fog employing conical micro-tip arrays, which have cactus spine-like shapes, and the hydrophilic cotton matrix [74].

Since it involves much effort to fabricate large branched wire structures, in this work, we desire to develop a new collector, which uses two large plates to collect water from fog. The development of such a collector is motivated by the feeding mechanism of a shorebird as discussed in Chapter 3. It has been reported that some feeding shorebirds with long thin beaks, such as phalaropes, are capable of driving liquid drops to move toward their mouths by opening and closing the beaks [29-33]. The drop movement is to transport the prey that may be contained in a liquid drop. This feeding process provides a new approach to control the movement of a water drop. As will be detailed in Section 4.3, the adoption of this method to develop an artificial collector results in three advantages in comparison with existing artificial collectors. First, unlike the mesh nets, the plates have much larger condensation areas, and the condensation water is actively transported to the desired locations. Thus, collection efficiency is improved. Second, it does not involve any hierarchical wire structures, which reduces the fabrication effort. Third and finally, since the manufacturing of plates is simple, it is easy to scale up the device to collect more water by using large plates.

4.2 Transportation mechanism and motivation

Squeezing and relaxing processes are used in the shorebirds to guide the drop movement [51,60-63]. Their physical mechanisms have been explored for the case when the trailing and leading edges of the drop are pinned, respectively, during the squeezing and relaxing processes [51,59]. In Chapter 3, we have further explored the situation when

both edges are not pinned during those processes [75]. Figure 4.1 gives a typical cycle of squeezing and relaxing processes that a shorebird uses to guide the unidirectional movement of a water drop. The corresponding demonstration is through an artificial beak that we developed. This artificial beak includes two nonparallel SiO_2-coated Si plates, which play a role similar to the shorebird beak. In the squeezing process (Figs. 4.1(a1) and 4.1(a2)), the water drop is pressed by the top plate into a pancake-like shape. In the relaxing process (Figs. 4.1(a3) and 4.1(a4)), the top plate is lifted up, the left edge of the drop may slightly move rightward, while the right edge has a relatively large leftward displacement. As a result, the whole drop is shifted toward the corner of the two plates at the end of the relaxing process. Repetition of these two processes results in the continuous movement of the drop toward the corner, which has been detailed discussed in Section 3.3.
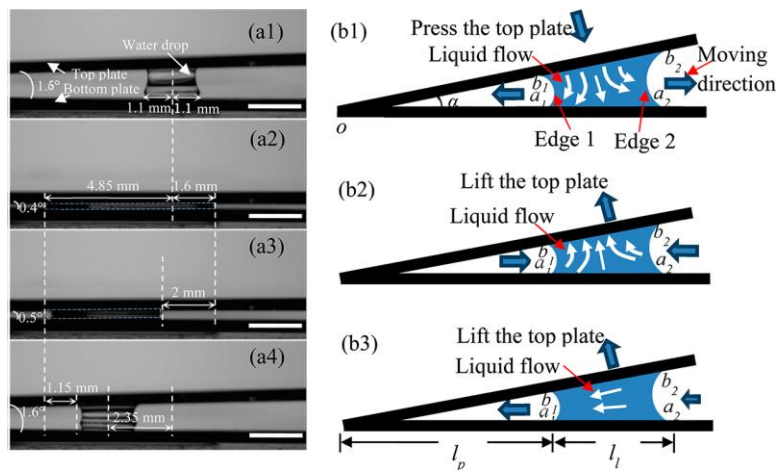
Figure 4.1 (a) Experimental results of squeezing and relaxing processes using two SiO_2 plates: (a1) squeezing of the drop, (a2) squeezed drop, (a3) relaxing of the drop, and (a4) relaxed drop. Scale bars in (a) represent 2 mm. (b) Cross-sectional schematics of flow patterns and edge movements of a lyophilic liquid drop during (b1) squeezing and (b2, b3) relaxing processes.

When water drops, which have condensed on plate surfaces, are squeezed between two plates, they should spread and merge together to form a large drop. By Eq. (3.14), it is readily shown that, for fixed α and l_p, ($p_{w2} - p_{w1}$) increases with the increase in l_l. Accordingly, the leftward movements of both Edges 1 and 2 that are illustrated in Fig. 4.1(b3) should also increase with the increase in l_l. This result indicates that the shifting effect increases with the size of the liquid drop. Thus, in comparison with individual condensed drops, the large drop formed by a group of them can be more easily transported to the plate corner, which provides a new approach to collect fog and further motivates us to develop a fog collector based on this approach.

4.3 Design of collectors and experimental setup

4.3.1. Design criteria

The new fog collector has a shape similar to the beak of a shorebird. It includes two large nonparallel plates (Fig. 4.2a). The collector is applied to collect fog through a two-step procedure. In the first step (Fig. 4.2a), the two plates are opened at a relatively large angle, facing the incoming fog flow. After condensed water drops grow to a certain size, the top plate is lowered down, and the water drops are subsequently driven toward the corner of the two plates through squeezing and relaxing processes (Fig. 4.2b), which is the second step. After a certain amount of water is accumulated in the corner, it is pumped away from the corner to start next round of fog collection (Fig. 4.2c).
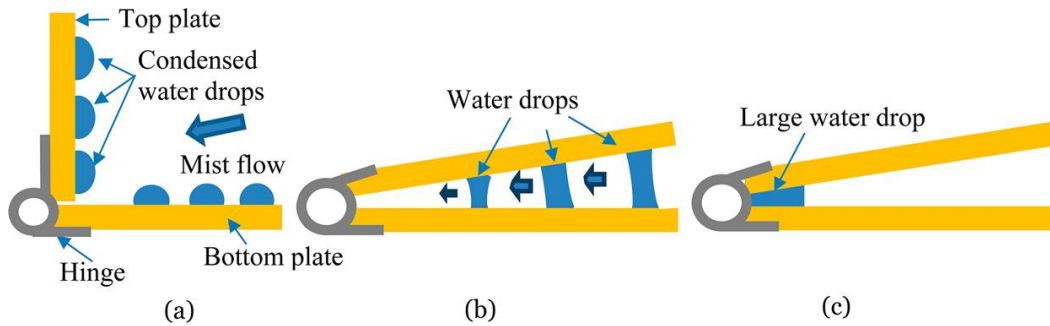
Figure 4.2 Process of collecting water: (a) open the two plates to collect fog; (b) squeeze and relax condensed water drops to drive them toward the channel located at the end of the bottom plate, and (c) after water drops stay in the corner, pump them away through the channel.

The major concern about a fog collector is its collection efficiency. The amount of water that is collected per unit time by our plate-based collector should increase with the increase in the following two aspects: the amount of water vapor that is condensed on the two plates, and the percentage of condensed water that can be transported to the corner of the two plates. The demand in the first aspect results in three design criteria: (i) the top plate should be oriented vertically to make its surface directly exposed to the mist flow, (ii) the bottom plate should be placed horizontally to avoid the loss of water drops due to gravity, and (iii) the plates should be as large as possible to have more surface area for water condensation. According to the first two criteria, the plate-based collector is designed as shown in Fig. 4.2(a). The selection of proper plate sizes for collectors based on the third criterion will be detailed in next sub-section.

The consideration of the second aspect yields two actuation criteria: (a) both small and large condensed drops should be transported to the corner of the two plates, and (b) to simplify the operation, a water drop should be translated as far as possible during each cycle of squeezing and relaxing to reduce the number of the actuation

cycles. These two actuation criteria have been employed in this work to determine the condensation period.

4.3.2. Plate sizes

Let l_1 and l_2 denote the dimensions of a plate, respectively, along the directions perpendicular and parallel to the intersecting line of the two plates. As justified below, the values of both l_1 and l_2 depend on the sizes of condensed drops.

Let α denote the relaxing angle that is needed to translate a water drop during a relaxing process, and set h to denote the maximum height that a water drop can have before it breaks during the separation of the two plates. It is considered that $l_1 \gg h$. According to simple geometry analysis, the value of l_1 is related to α and h by

$$l_1 \le \frac{h}{\alpha}. \tag{4.1}$$

Obviously, h increases with the increase in the drop size. Also, it has been demonstrated that the translation of a liquid drop per actuation cycle increases with the increase in the drop size [75]. Thus, large condensed drops are desired to have a large value of l_1.

In principle, the value of l_2 can be as large as possible. In reality, it is limited by fabrication and assembly errors. These errors may create a gap between the two plates when these plates are put together. Accordingly, if the height of a water drop is smaller than the gap, then a water bridge could not be formed between the two plates to transport the drop. Hence, large condensed drops are also desired to have a large value of l_2.

On the other hand, in a very dry environment, in which only small water drops may exist, the values of l_1 and l_2 should be reduced accordingly to ensure that water bridges could be formed between two plates to transport the corresponding water drops.

When the radius of a condensed water drop exceeds the capillary length of water, which is 2.7 mm, gravitational effect dominates. According to ref. 69, the height of such a large drop is:

$$e = 2l\sin(\frac{\theta}{2}),$$ (4.2)

where l denotes the capillary length of water, and θ is the apparent contact angle of the water drop. e is also the maximum height that a water drop may have. Hence, the fabrication and assembly errors of the two plates should be less than e. Also, we should wait until the condensed drop has a radius larger than 2.7 mm before the start of the collection step. Once the height reaches the value of e, the continuous condensation does not increase the height of the drop, while it should increase the lateral dimension of the drop.

There exist three basic stages of condensation [76,77]: initial, intermediate, and large drop formation. In these three stages, the average drop radii, R, are related to time, t, as $R \sim t^{1/3}$, $R \sim t$, and $R \sim t^{1/2}$, respectively. Thus, drops grow in a fast manner in the second stage, and the growth is slowed down in the third stage. Accordingly, the best timing to start the collection step is at the beginning of the third stage. On the other hand, the observation of the results in refs. 76 and 77 indicates that the time duration of each stage depends on the substrate geometry, substrate coatings, and the incoming fog flow. These factors are experimentally examined in this work.

In addition, by Eq. (4.2), e increases with the increase in θ. This implies that a more hydrophobic surface will result in a high value of e. On the other hand, a water drop actually moves away from the corner of the two plates in the hydrophobic case (i.e., $\theta > 90^0$). In contrast, when θ is close to 0°, the drop may move toward the corner of the plates by itself without any actuation [51,75]. This implies that, for the transporting

purpose, more hydrophilic surfaces are desired. Accordingly, a contradiction occurs regarding the value of θ. To find an optimal value of θ in terms of both the plate sizes and collection efficiency, we test glass plates, SiO_2-coated Si plates, and SU-8-covered Si plates. The corresponding values of θ on these plates are 18 $\pm 2^o$, 42 $\pm 2^o$ and 82 $\pm 2^o$, respectively. For simplicity, the latter two plates are called "SiO_2 plate" and "SU-8 plate", respectively. The three types of plates have rectangular shapes with the approximately same dimensions of 4.2 x 2.1 x 0.05 cm^3 (length x width x thickness).

4.3.3. Experimental setup for a small collector

Two collectors have been built. A small one was first built and tested. As shown in Fig. 4.3, the small collector included two identical plates. The top plate was lifted or lowered down using a micromanipulator. At room temperature (22 °C $\pm$ 1 °C), a humidifier (model: EE-5301, Crane USA Co.) was employed to generate a mist flow (Fig. 4.3). A plastic tube was used to guide this mist flow. The tube had a diameter of 2 cm. It was comparable to the width of a plate. The relative humidity was 100% in the tested area. In the designed case (Fig. 4.2a), the mist flow has a large incident angle on the top plate. However, the small collector was used to examine the minimum amount of vapors that might be condensed on a plate. It was expected that this would occur when the mist flow was parallel to this plate. Thus, in the small collector, the mist flow that came out of the tube was approximately along the horizontal direction, and formed an angle of 15° with the bottom plate. The flow fully covered the bottom plate, while had much less contact with the top plate.
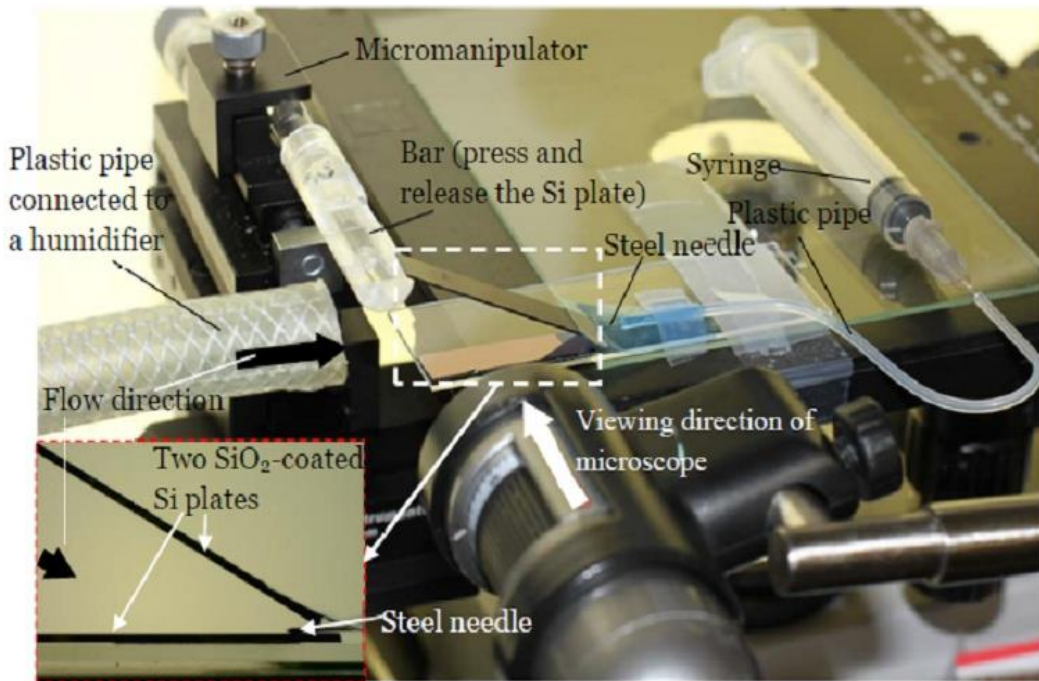
Figure 4.3 Experimental setup for water collection

The humidifier had been turned on for 1 min to ensure that the flow rate had been steady before the flow was pointed to the bottom plate, followed by the recording of the condensation and collection processes through an optical microscope. A steel needle was inserted at the corner of the two plates to collect water accumulated over there with the aid of a syringe that was connected to the needle. Tests were done on the three types of plates to find: (i) the relation of the drop sizes with the condensation times, (ii) the number of actuation cycles needed to completely transport condensed drops from the plates to their corner, and (iii) the values of α and l_1. On the basis of the understanding gained on these tests, a large collector was subsequently designed and built to collect a large amount of water. The design and setup of the large collector will be detailed in Section 4.4.3.

4.4 Experimental results and discussions

4.4.1. Condensation

Fig. 4.4 shows the time evolution of average diameters of condensed water drops after the bottom plate has been exposed to the mist flow from 0 to 45 min. After 8, 14, 16 min, the radii of the condensed drops on glass, SiO_2, and SU-8 plates, respectively, have exceeded the capillary length of water. According to the relationship of the drop sizes with time, we divide condensation process on each type of plates into three stages: initial, intermediate, and large-drop formation. The average radius of the drop is below the capillary length of water in the initial stage, while it is above in the other two stages. However, the time durations and drop growth rates in these three stages vary with the type of plates. Different from what was reported in refs. 76 and 77, except for the intermediate stage, the drop sizes in the other two stages also approximately linearly increased with time. On the other hand, as reported in refs. 76 and 77, the drop growth rate was the largest in the intermediate stage.

Some phenomena observed on each type of plates are described below. For the glass plates, in the initial stage (t ≤ 8 min, Fig. 4.4a1), drops nucleated, and tiny drops appeared and were densely distributed on the plate (Fig. 4.4b). In the intermediate stage (8 min<t<20 min, Figs. 4.4a2 and 4.4b), drops gradually increased their sizes with a higher rate of 1.6 mm/min than the one in the first stage (0.2 mm/min) due to coalescence of and condensation on pre-existing drops. In the stage of large drop formation (t ≥ 20 min, Fig. 4.4a3), drops had diameters as large as 24.0 mm after 24 min, and tiny drops were also seen between the large ones (Fig. 4.4b). In this stage, the growth rate of condensed drops decreased to 0.3 mm/min. When the glass plate was exposed to the mist flow for more than 30 min, the sizes of some drops were even beyond the width of the plate. Correspondingly, these drops spilled out of the plate.

Two different phenomena were observed on the SiO_2 plates in the initial (t < 14 min, Fig. 4.4a4), intermediate (14 min <t< 28 min, Fig. 4.4a5), and large-drop formation (t $\geq$ 28 min, Fig. 4.4a6) stages. When the bottom SiO_2 plate was exposed to the mist flow for 30 min, the condensed drop reached the edge of the plate but not spilled out of the plate due to the relatively larger contact angle than the glass plate (Fig. 4.4c). The fastest growth rate of condensed drop, which occurred in the intermediate stage, was 0.78 mm/min, which was about half of its counterpart in the case of glass plates. Drops had diameters as large as 15.9 mm after 36 min.

The condensation process on the SU-8 plates has both longer initial and intermediate stages (t $\leq$ 16 min, and 16 min<t<36 min, respectively, Figs. 4a7 and 4a8) than those on glass and SiO_2 plates. In the stage of large drop formation (t $\geq$ 36 min, Fig. 4.4a9), drops had diameters as large as 8.6 mm after 36 min, and tiny drops were also seen between the large ones (Fig. 4.4d). The fastest growth rate of condensed drop, which occurred in the intermediate stage, was 0.2 mm/min, which was about one third of its counterpart in the case of SiO_2 plates.

The differences among the phenomena on the three types of plates are considered to be induced by the different contact angles on the plates. When the plate surface is more hydrophilic, the condensed drops are easy to spread on this surface, making their diameters increase at a higher rate. Accordingly, on the glass plates, the initial and intermediate stages last shortest periods, while their drops have the smallest heights in the large-drop formation stage.
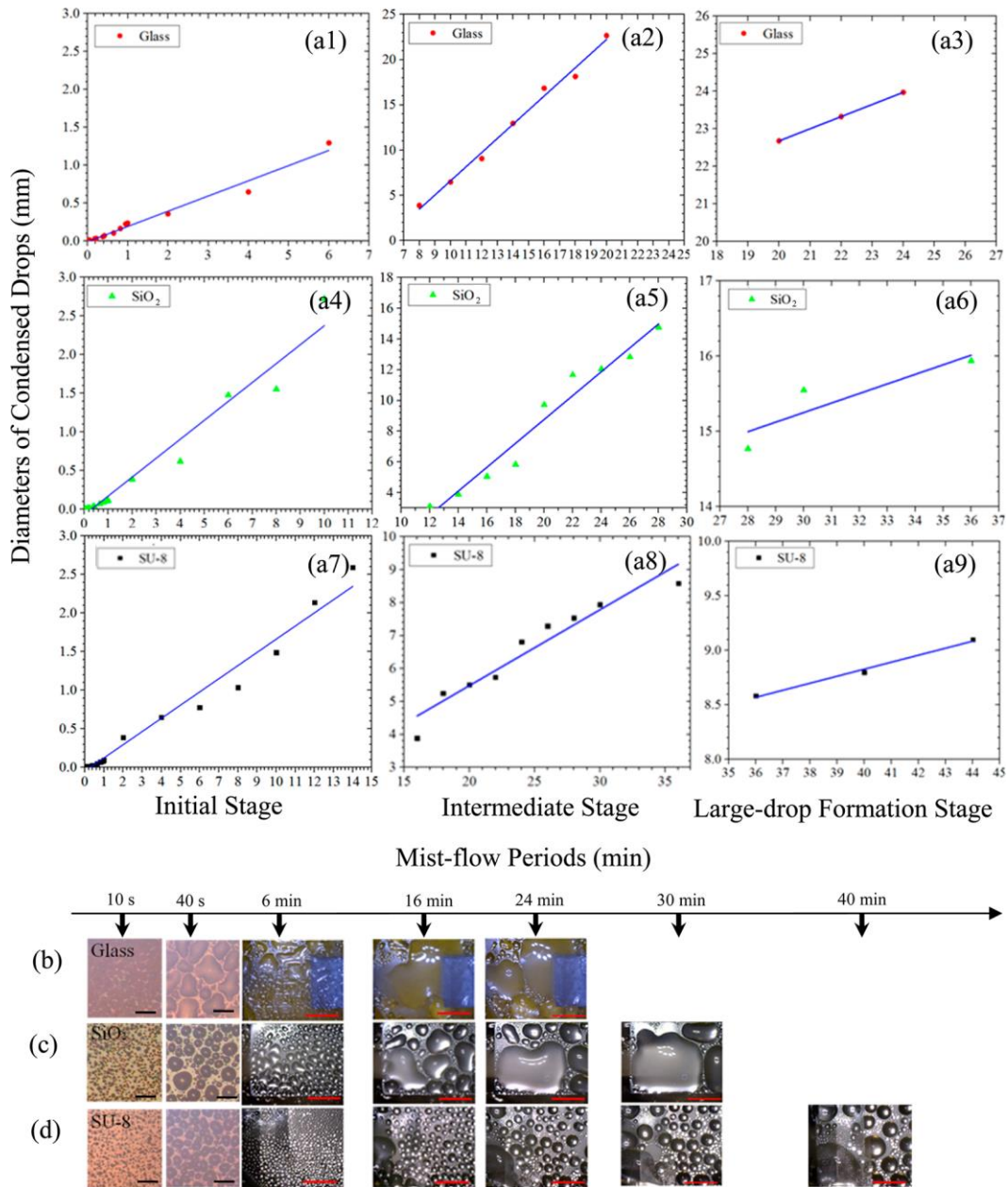
Figure 4.4 (a) Time evolution of diameters of condensed drops on the different plates,
respectively, after 1−45 min. (b−d) Water drops on the glass, SiO$_2$, and SU-8 plates,
respectively, after 10 s, 40 s, 6, 16, 24, 30, and 40 min condensation periods,
respectively. Black and red scale bars represent 100 μm and 10 mm, respectively.

61

4.4.2. Transport of condensed drops

For each type of plates, water was collected five times when condensation lasted 1, 5, 10, 15 and 30 min, respectively, under the same experimental conditions as discussed in Sub-section 4.4.1. Four tests were done each time, and the average value was given in Fig. 4.5a. For easily identifying data, the error bars were not added to this figure. Instead, the errors are provided when the corresponding data are indicated in the following text. As indicated in Sub-section 4.3.2, the best time to start the transport of the condensed water drops is still at the beginning of the stage of large-drop formation. This stage starts at t=20, 28 or 36 min on glass, SiO_2 or SU-8 plates. Given that water began to spill out of the glass plates at t=30 min, the longest condensation period was chosen to be 30 min in our tests on the small collector.
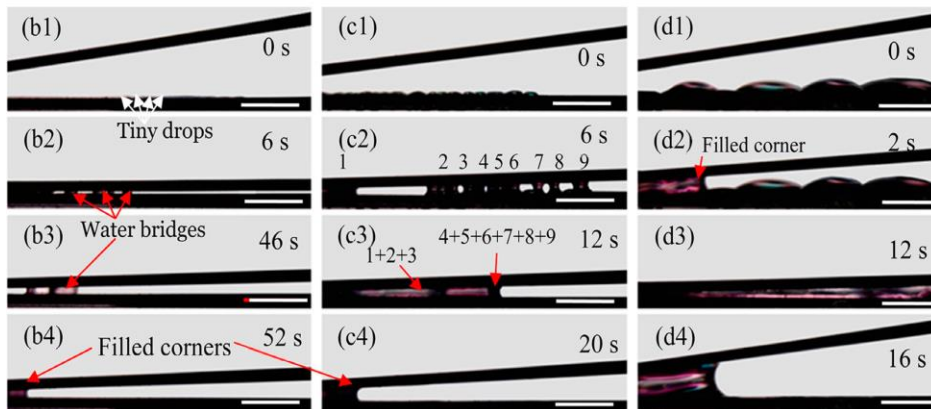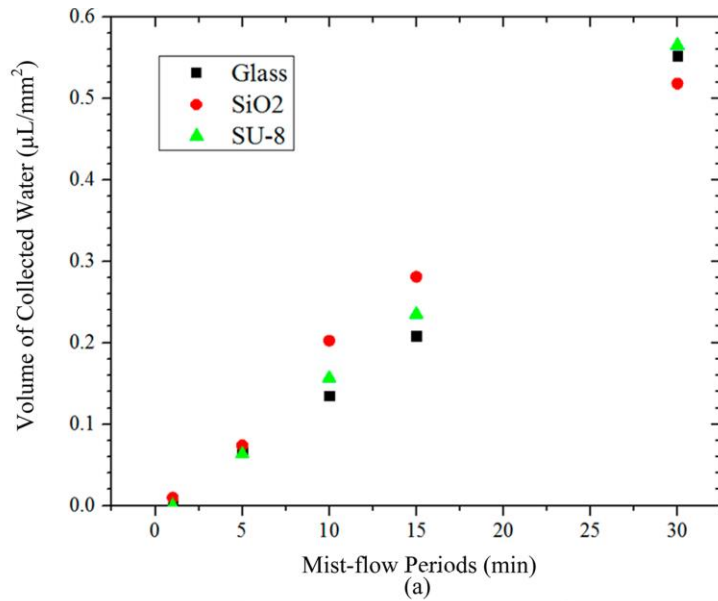
Figure 4-5 (a) Volumes of collected water per mm^2 corresponding to different mist-flow periods. Squeezing and relaxing of water drops after mist flows using SiO$_2$ plates for (b) 1, (c) 5, and (d) 30 min, respectively. (b1), (c1), and (d1), before the top plate is lowered down; (b2), (c2), and (d2), press the drops; (b3), (c3), and (d3), relax the drops; and (b4), (c4), and (d4), after 1 or more cycles, the corner of two plates is filled with water. Numbers in (c2) and (c3) represent different water drops, and "1 + 2 + 3", for example, means that drops 1, 2, and 3 are merged into one drop. Scale bars in (b−d) represent 2 mm.

Three interesting points were observed from Fig. 4.5(a). First, the collected water for each type of plates approximately has a linear relationship with the condensation time. This is considered reasonable, since in our tests the incoming mist flow is steady. Accordingly, the amount of the absorbed water vapor should linearly increase with time. The same point is applied to the finally collected water.

Second, there are relatively large differences among the collected amounts of water on the three types of plates for the cases of 10- and 15-min condensation periods. For example, in the 10-min case, the total amounts of water collected per unit area on the glass, SiO_2, and SU-8 plates were 0.134 ± 0.003 $\mu L/mm^2$, 0.203 ± 0.032 $\mu L/mm^2$, and 0.157 ± 0.030 $\mu L/mm^2$, respectively. The largest difference was about 0.07 $\mu L/mm^2$. After 10- or 15-min condensation, relatively small drops on the SU-8 plates are formed in comparison with those on another two types of plates (Fig. 4.4d). Consequently, the top SU-8 plate was pressed harder to ensure all the condensed water drops could form bridges, making some drops located near the edge spill out of the plate. In addition, glass plates have relatively high hydrophilicity. Part of water still sticks to the plate surface after a cycle of squeezing and relaxing processes. Hence, the loss of water during the collection process makes SU-8 and glass plates collect less water.

Third and finally, the differences in the amounts of collected water were smaller in another three cases. After the 30-min condensation, the total amounts of water collected per unit area on the glass, SiO_2, and SU-8 plates did not have much difference, which were 0.55 ± 0.07 $\mu L/mm^2$, 0.52 ± 0.08 $\mu L/mm^2$, and 0.56 ± 0.02 $\mu L/mm^2$, respectively, since the amount of lost water previously mentioned in the second point was much smaller than the totally collected water.

Three points were further observed during the squeezing and relaxing processes (Figs. 4.5b-d). First, water bridges were formed when the top plate was lowered down,

even in the 1-min case (Fig. 4.5b2). It was found that neighboring water drops were merged to form a large drop, when they elongated and contacted each other due to the pressing of the top plate (Figs. 4.5b3). This result implies that the squeezing process actually increased the size of water drops. Second, during the relaxing process, a water bridge might further merge with its neighboring bridges to form a larger one (Figs. 4.5c3 and 4.5d3). According to the result of ref. 75, the shifting distance of a water bridge increases with the drop size. Consequently, due to different shifting distances, a large water bridge may catch up and thus merge with a small bridge in front of it during the relaxing process. The first two points actually aided in the transport of water during a processing cycle. Third, the needed actuation cycles decreased with the increase in the drop sizes. Take the tests on the SiO_2 plates as an example. It took 22 cycles to translate all the drops collected during the 1-min case, 4 cycles for the 5-min period, 1-2 cycles for the 10-min period, but only 1 cycle for both 15- and 30-min cases. As indicated in the first two points, the pressing and relaxing processes result in the coalescence of drops. Large drops were formed in the 15- and 30-min cases, and they were merged into a huge one, which was capable of moving to the corner of the two plates during a single actuation cycle (Fig. 4.5d(3)). However, due to relatively small sizes of the condensed drops in another three cases, the merged drops were still not large enough to move to the corner during a single actuation cycle (Figs. 4.5(b3) and 4.5(c3)). Thus, in the first three cases, more than 1 actuation cycle were needed to translate all the collected water to the corner.

4.4.3. Design and testing of the large collector

As discussed in Sub-section 4.4.2, in the 30-min case, the three types of plates collected about the same amount of water, and they all just needed a single actuation cycle to translate all the collected water to the corner. Also, during this actuation process, the condensed drops were all merged together to form a thin film in the squeezing

process on each type of plates, making the relaxing degree less than 1° for the whole film to move to the corner. Therefore, we did not see much difference in the fog-collection efficiencies and relaxing angles of the three types of plates.

Next, we compare the plates in the case of collecting a single drop. As shown in Fig. 4.4, the average diameters of condensed drops are 22.7, 15.6, and 8.6 mm at the desired collection times of 20, 28, and 36 min on glass, SiO_2, SU-8 plates, respectively. Accordingly, the drops with the same diameters were placed between the corresponding plates. The break heights of water bridges were measured as 5.1, 6.0, and 5.5 mm, respectively, on glass, SiO_2, and SU-8 plates. Furthermore, when the relaxing angle was 1.2°, the drops began to move toward the corner on each type of plates. According to Eq. (1), the maximum values of l_1 on the three types of plates did not have large difference, which were 24, 29, and 26 cm, respectively.

We then focus on the drop heights on glass, SiO_2, and SU-8 plates at the end of condensation periods, since, as previously discussed in Sub-section 4.3.2, these heights affected the values of l_2. After a 36-min condensation period, the heights of drops on glass, SiO_2, and SU-8 plates were measured to be 1.6, 2.5, and 3.2 mm, respectively. Hence, SU-8 plates were chosen for the large collector. These plates were made by coating SU-8 on glass plates. In this collector, l_1 was set to be 26 cm as previously discussed, and l_2 was temporarily chosen to be 10 cm because of the availability of such plates. The thickness of the plates was 0.2 cm.

As shown in Fig. 4.6(a), the setup of the large collector is similar to what was illustrated in Fig. 4.2. On the other hand, it has two differences from the one for the small collector (Fig. 4.3): (i) to create a relatively uniform fog environment using our humidifier, instead of an open space, the large collector was placed in a closed glass chamber with

dimensions of 40 x 30 x 30 cm^3; and (ii) the mist flow did not directly blow the two plates, and it came in the glass chamber through a top opening.
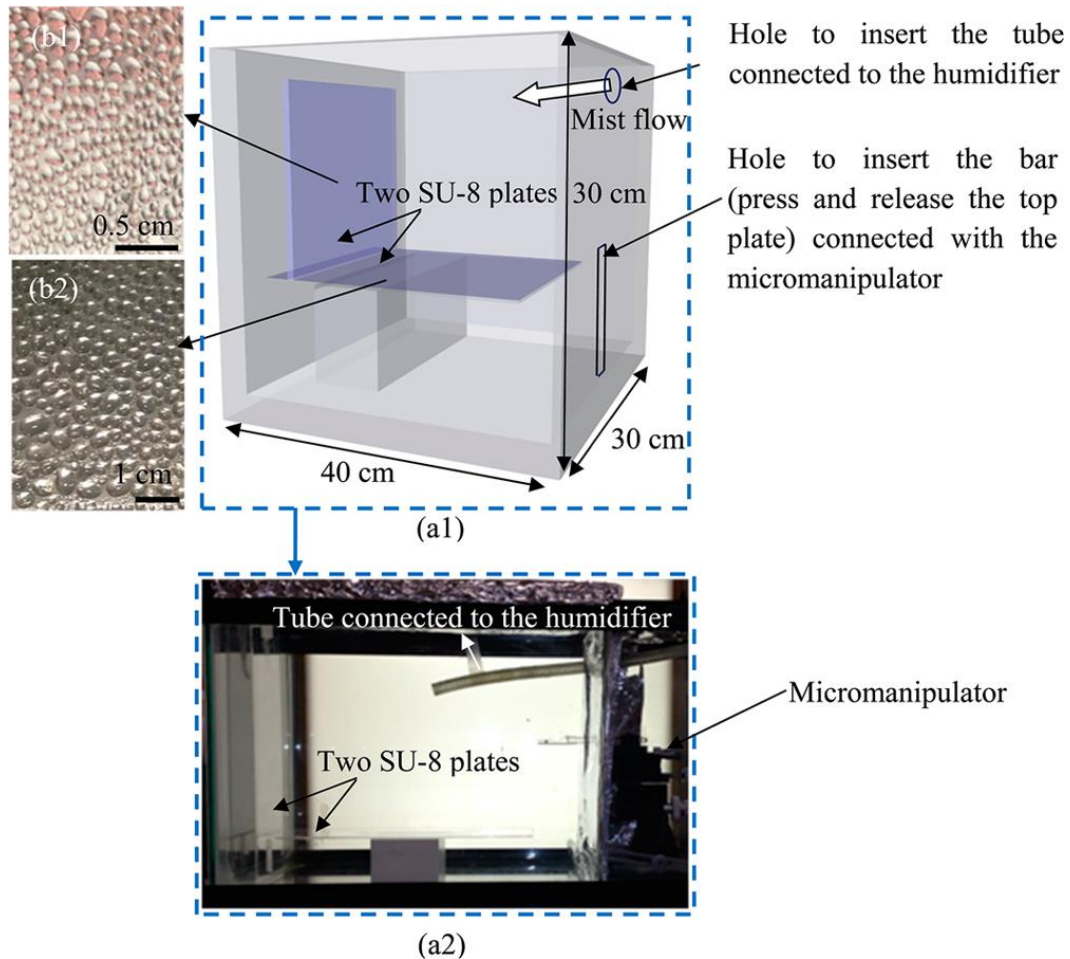
Figure 4.6 (a) Experimental setup for water collection by two large SU-8 plates with dimensions of 26 × 10 × 0.2 cm3, and (b) water drops on the surfaces of two plates after 36 min condensation.

As shown in Fig. 4.6(b), the average diameters of condensed drops after the 36-min condensation period were about 1 and 5 mm on the surfaces of top and bottom plates, respectively. During condensation, it was observed: (i) large condensed drops moved down from the top plate to the corner of the two plates due to gravity; and (ii) only

smaller ones remained on the top plate. Accordingly, the average diameters of condensed drops were different on the surfaces of the two plates. In addition, the average drop sizes on these two plates were smaller than the one in the case of the small collector, which was 8.6 mm. This difference implies that the vapor densities around the two plates of the large collector were lower than that surrounding the bottom plate of the smaller collector, due to the fact that the two plates were not directly blown by the incoming mist flow.

Four tests were done to examine the fog-collection capability of the large collector during a 36-min mist flow. Only 1 cycle of squeezing and relaxing was needed to translate all the condensed drops to the corner of the plates. It took no more than 3 s to complete this cycle, which was much shorter than the condensation period of 36 min. Therefore, although no condensation is performed during the squeezing and relaxing processes, as far as time is concerned, these processes have little influence on water collection. The total amount of collected water was about 15.8 ± 2 mL. The amount of water collected per unit surface area was calculated to be 0.30 μL/mm^2. As expected, this value was less than its counterpart in the case of the small collector, which is about 0.56 μL/mm^2 after 30-min condensation.

As discussed in Sub-section 4.3.2, the plate sizes should decrease with the decrease in the humidity level in an environment to effectively transport water drops. In a desert, the fog event normally occurs in the late night and early morning due to relatively low temperature during these periods. It has been reported that, in Chili's desert, the fog can bring water as much as 1.5 μL/mm^2 per hour in the morning [78]. This amount is 2.5 times higher than what has been collected using the large collector during a 1-hour period, implying large water drops may still be formed on the plates in this desert. Accordingly, a large collector may be effective as well to collect fog over there.

4.4.4. Comparison of fog-collecting efficiencies

Fog-collecting efficiencies have been compared in ref. 12 among fog-basking beetles, Namib dune bushman grasses, and metal wires. In their case, the temperature was kept between 10 and 15 °C. A humidifier produced 325 mL fog per hour with a speed of 0.1 m/s. All the samples were placed at 23° to the horizontal direction. These samples collected 0.25, 0.48 and 0.61 $\mu L/mm^2$, respectively, during the 120-min periods. Our tests on the smaller collector were performed under similar experimental conditions. The condensation and collection were done at room temperature (22 °C $\pm$ 1 °C). The incoming mist flow had the angle of 15° with the bottom plate. It had a speed of 0.08 m/s. The big difference was that the amount of fog produced by our humidifier per hour was 81 mL, which was less than that of ref. 12. In the 30-min case of the smaller collector, the average collected water per unit surface area of the bottom SU-8 plate is 0.56 $\mu L/mm^2$. When our value is scaled by 4 times from 30 to 120 min (i.e., repeat the 30-min case 3 times), the collected water per unit area is 2.24 $\mu L/mm^2$. It is about 9.0, 4.7 and 3.7 times, respectively, as large as the ones of beetles, grasses and metal wires. It is considered that the active transport of condensed water has the main contribution to the higher collection efficiency of the small collector, which ensured that all the water condensed on the artificial collector was almost collected. In the cases of fog-basking beetles, Namib dune bushman grasses and metal wires, as discussed in Section 4.1, the condensed water is translated by gravity and capillary force, which is a passive method and may not be capable of transporting all the condensed water.

Furthermore, during the 120-min periods, a beetle, a grass and a metal wire, respectively collected 0.06, 0.11 and 0.13 mL volumes of water, which are about 33, 18 and 15 times less than what was collected by the small collector if our result is also scaled from 30 to 120 min. Part of the difference is caused by the larger condensation

surface area of the small collector. The total surface area of the small collector, which only counts the bottom plate surface, is 882 mm^2. It is larger than the ones reported for individual beetles, grasses and metal wires [12], which are 245, 253, and 220 mm^2, respectively. Therefore, in comparison with well-known fog-harvesting animal and plant and an artificial collector, our small collector has demonstrated much higher efficiency in fog collection. This comparison also indicates the importance of both introducing plates (to gain large collection areas) and using the squeezing and relaxing actuation (for actively transporting condensed drops). It is considered that directly testing beetles and grasses in our experimental conditions should give better comparison between them and our collectors. Due to lack of these desert animals and plants, they are not tested in this work.

Although the amount of water collected by the large collector per unit area is less than the one harvested by the small collector due to different experimental conditions, when our value is scaled from 36 to 120 min, it is still about 3.4, 1.8 and 1.4 times, respectively, as large as the ones of beetles, grasses and metal wires. In addition, due to its large surface area, which is 52,000 mm^2 and counts the surface areas of both top and bottom plates, the scaled amount of water collected by the large collector is about 878, 479, and 405 times more than what was collected by individual beetles, grasses or metal wires.

Moreover, vertically oriented plates with hydrophobic or hydrophilic surfaces have been previously tested in refs. 79 and 80 for their fog-collecting efficiencies. Due to gravity, large drops that are condensed on a plate can be drained to a container, which is located under the plate. During a 30-min period, the water collected per unit area on a graphene-coating (hydrophobic) surface is 0.148 µL/mm^2 [79], while it is 0.1 µL/mm^2 on a hexamethyldisiloxane (superhydrophilic) surface with the drainage path [80]. They are

lower than what has been collected on either our small or large collector. However, due to different experimental conditions, such as humidity and temperature, this comparison is not accurate.

In the cases of refs. 79 and 80, tiny drops cannot be drained, since their gravity is less than the resistance force induced by the contact angle hysteresis. Subsequently, not all condensed drops can be collected. Nevertheless, in this work, due to the aid of the squeezing and relaxing processes, such tiny drops can still be collected. Thus, under the same experimental conditions, our collectors should have higher collecting efficiencies when the same plates are used to collect water.

A set of experiments has been done to validate this point. The corresponding experimental setup is similar to the one shown in Fig. 4.6. On the other hand, there are three differences from the tests on the large collector. First, the glass, SiO_2 and SU-8 plates that have been used in the small collectors were adopted in the tests, and in each test only a single plate was vertically put inside the chamber. Second, as in the case of the small collectors, the condensation duration in every test was 30 min, instead of 36 min. Third, the water was collected through two steps, instead of a single one. In the first step, water was collected from the bottom of the vertical plate at the end of the condensation period. In the second step, the water that still remained on the vertical plate was collected using the squeezing and relaxing processes, in which the vertical plate served as the top plate while a dry plate functioned as the bottom one.

In our tests, the amounts of water collected from the bottoms of glass, SiO_2 and SU-8 plates at the end of the 30-min condensation period were 0.315, 0.397 and 0.406 $\mu L/mm^2$, respectively. After the application of the squeezing and relaxing processes, additional 0.148, 0.072 and 0.075 $\mu L/mm^2$ were collected from these plates, separately. These results indicate: (i) totally 0.463, 0.470 and 0.482 $\mu L/mm^2$ are collected from glass,

SiO$_2$ and SU-8 plates, separately, which also do not vary much with the plates as in the 30-min case of the small collector; (ii) 68%, 85% and 84% are, respectively, collected from the three plates during the condensation process, which occurs due to the effect of gravity; and (iii) the remaining 32%, 15% and 16% of condensed drops can be further collected using the squeezing and relaxing processes. Accordingly, the adoption of the active transportation approach improves the collecting efficiency.

In addition, another two points can be observed from these results. First, the wettability of the surface highly influences the collecting efficiency in the first step, which agrees with what has been observed by other researchers [79,80]. Second, the introduction of squeezing and relaxing actuation ensures that almost all condensed drops can be collected, which may be a major reason why the three types of plates do not have much difference in the amounts of finally collected water.

4.5 Summary and conclusions

In this work, motivated by the feeding mechanism of a shorebird, we have developed a plate-based collector to harvest water from fog and dew. As in the case of the shorebird, squeezing and relaxing processes have been applied to facilitate the transport of condensed water drops from the plate surfaces to the corner of two plates. We have explored the condensation and collection of a small version of the artificial collector, and found it was much efficient than desert animal and plants due to the active transport of condensed water, which ensured that all the water condensed on the artificial collector was almost collected. Based on these results, we further developed a large collector. Because of its relatively larger surface areas, 15.8 mL water was collected during a condensation period of 36 min.

Chapter 5

Separation of Oil from a Water/oil Mixed Drop using Two Non-parallel Plates

In this work, we have developed a simple approach to separate oil from a μL-scaled water/oil mixture by squeezing the mixture using two non-parallel plates. Three pairs of plates with Teflon, SU-8 and SiO_2 coatings, respectively, are used in the tests, and all of these plates are capable of separating the water/oil mixed drops. 95.5% silicone oil and 97.0% light mineral oil have been collected from their corresponding mixtures with water through the pair of Teflon plates. Furthermore, on the basis of pressure difference inside a liquid drop, theoretical models have been developed to interpret the corresponding mechanisms of the separation process, as well as the observed phenomena. To judge whether two immiscible liquids could be separated using the developed approach, a sufficient condition has also been derived, which includes three theoretical relations. The sufficient condition is subsequently validated by experiments. This condition also provides criteria for choosing a good plate coating. Such a coating should ensure: (i) the oil wets the plate surface with a relatively large contact angle, and has small contact angle hysteresis; and (ii) advanced contact angle that water/oil interface forms on the plate surface is larger than 90º.

5.1 Introduction

Quite a few approaches have been developed to separate a mixture of two immiscible liquids according to their difference in boiling points, mass densities, or lyophobicities. When two liquids have appreciable difference in their boiling points, the liquid with the lower boiling point may be separated from a mixture of the two liquids by heating the mixture to this boiling point. At such a temperature, that liquid becomes vapor, getting separated from the other liquid. Due to the difference in the mass

73

densities, two liquids may also form two separate layers in a container. These two layers may be separated by letting the bottom one flow out through the bottom of the container.

Mesh structures are also applied to handle two immiscible liquids based on their different lyophobicities. For instance, mesh films, which are covered or constructed, for example, by carbon nanotubes [81], carbon nanotube networks [82], nanostructured hydrogel coatings [83], nanocomposites [84], TiO_2 nanowires [85], kapok fibers [86], or $Cu(OH)_2$ nanowires [87], have been applied to separate the mixtures of water and oil based on different wetting properties of these two liquids on the modified mesh films.

The aforementioned approaches are usually employed to handle a large amount of mixtures. On the other hand, it is not clear whether they could be employed to separate a µL-scaled mixture with high separation efficiency. Such separation may be needed in the analysis of the components in a mixture when only a small amount of the mixture is available. Another potential application of this separation is liquid-liquid microextraction (LLM). The LLM utilizes the fact that the solute has different solubilities in two different immiscible liquids. Accordingly, the solute could be transferred from one liquid (donor) to the other (extractant). After the extraction is completed, the extractant has to be separated from the mixture of the two liquids. In the LLM, only a small amount of an organic solvent (water-immiscible liquid) is employed to extract the solute from water to decrease the quantities of harmful chemicals and organic solvents used or to avoid exposure of too much toxic organic solvents in the air. Several separation techniques have been developed for the LLM [88-90]. In refs 88 and 89, a fiber is first impregnated with a small amount of organic solvent, and then immersed into the water with solute to extract the solute into the fiber. Moreover, electrowetting on dielectric (EWOD) is also used to extract the solute [90]. The volumes of two immiscible liquid drops tested are both 200 nL. These two drops are controlled to mix and separate on an

74

EWOD digital microfluidic chip. In this work, we have developed a new approach to handle a small amount of mixtures based on different wetting properties of two immiscible liquids. This approach is simple to apply, and only requires the use of a pair of non-parallel plates.

The behaviors of liquid drops between two non-parallel plates have been previously explored by Concus and Finn, together with their collaborator [49,50,53,54,56] (see ref 50, for example, for a summary of their works). An angle inequality has been previously derived to judge whether a liquid drop fills the corner of two non-parallel plates [49,50]. This angle inequality was also obtained in one of our previous works during the process of exploring the condition for a liquid drop to fill microchannels [23]. According to the angle inequality, a lyophobic liquid drop may not fill the corner of two non-parallel plates, after it is put between them. Otherwise, the filling may happen. These different filling results imply that, when two immiscible liquids in a mixture have different wetting properties, they may be separated simply using two non-parallel plates. This may provide a new approach to separate a mixed drop. Accordingly, it is explored in this work.

The outline of this article is as follows. Experimental results are presented and discussed in Section 5.2. In Section 5.3, theoretical models have been developed to explain these results, followed by experimental validation. Finally, this work is summarized and concluded in Section 5.4.

5.2 Experimental results and discussions

5.2.1. Contact angles

Water and silicone oil (Alfa Aesar Co., MA, USA) are tested in the new approach. Three pairs of non-parallel glass or silicon plates are used to separate their mixed drops. The three pairs of plates are covered by Teflon, SiO_2 and SU-8 films, respectively. For simplicity, they are called Teflon, SiO_2 and SU-8 plates, separately. SU-8 is a negative

photoresist. It can be patterned to desired shapes using ultra-violet lithography. It has functioned as a good structural material in microsystems, such as in gears [91], boats [92-94] and flotillas [95,96]. After a liquid drop is put on a plate, the side view of the corresponding equilibrium state is imaged through an optical microscope. The advanced and receding contact angles are measured on the plate by increasing and decreasing the volume of the drop, respectively, till this drop starts to move. The advancing contact angles of water on Teflon, SiO_2 and SU-8 plates are measured to be 125°, 67° and 92°, respectively (Table 5.1). The receding contact angles are 120°, 42° and 55°. The advancing contact angles of oil on these plates are 41°, 2° and 2°, respectively, while the receding contact angles are 39°, 1° and 1°.

Table 5.1 Advancing and receding contact angles of water, silicone oil and light mineral oil on Teflon, SiO_2, and SU-8 Plates, Respectively

	viscosity (mm^2/s) at 25 °C		SiO_2 plate	SU-8 plate	Teflon plate
water	1	receding contact angles (θ_{rw})	42°	55°	120°
		advancing contact angles (θ_{aw})	67°	92°	125°
		contact angle hysteresis ($\theta_{aw} - \theta_{rw}$)	25°	37°	5°
silicone oil	40	receding contact angles (θ_{ro})	1°	1°	39°
		advancing contact angles (θ_{ao})	2°	2°	41°
		contact angle hysteresis ($\theta_{ao} - \theta_{ro}$)	1°	1°	2°
water/silicone oil mixture		receding contact angle of water/silicone oil interface (θ_{rm})	112°	106°	141°
		advancing contact angle of water/silicone oil interface (θ_{am})	158°	165°	155°
light mineral oil	20	receding contact angles (θ_{rg})	15°	27°	60°
		advancing contact angles (θ_{ag})	16°	27°	62°
		contact angle hysteresis ($\theta_{ag} - \theta_{rg}$)	1°	0°	2°
water/light mineral oil mixture		receding contact angle of water/silicone oil interface (θ_{rmg})	133°	116°	147°
		advancing contact angle of water/silicone oil interface (θ_{amg})	155°	154°	158°

5.2.2. Structure of a mixed drop

The mass density of silicone oil is 963 Kg/m^3. It is slightly lower than that of water, which is 10^3 Kg/m^3. To explore possible profiles of a mixed drop on a plate, three methods have been applied to form a mixed drop of the two liquids (Fig. 5.1). These methods differ in the order or the location that water and oil drops are placed on the plate. In the first method (Figs. 5.1(a1) and 5.1(a2)), an oil drop is directly put on the top of a water drop. Subsequently, the oil spreads and surrounds the water drop. Meanwhile,

a thin layer of oil still covers the whole water drop. Although the contact angles of water and oil vary with the plates, the mixed drops made on the three types of plates have the same structures. In a mixed drop, a water core, which is in the form of a drop, is wrapped by an oil drop (Fig. 5.1d). In the second method (Figs. 5.1(b1) and 5.1(b2)), a water drop is directly put on the top of an oil drop, while in the third approach, oil and water drops are placed on a plate side by side (Figs. 5.1(c1) and 5.1(c2)). It is interesting to observe that the resulting mixed drops in these two methods also have structures similar to that produced using the first method (Fig. 5.1d). This result indicates that the structure of a mixed drop does not depend on the way of mixing the oil and water. In this work, the mixed drops formed using the first method are used in the subsequent tests, and have volumes in the order of 20 µL.
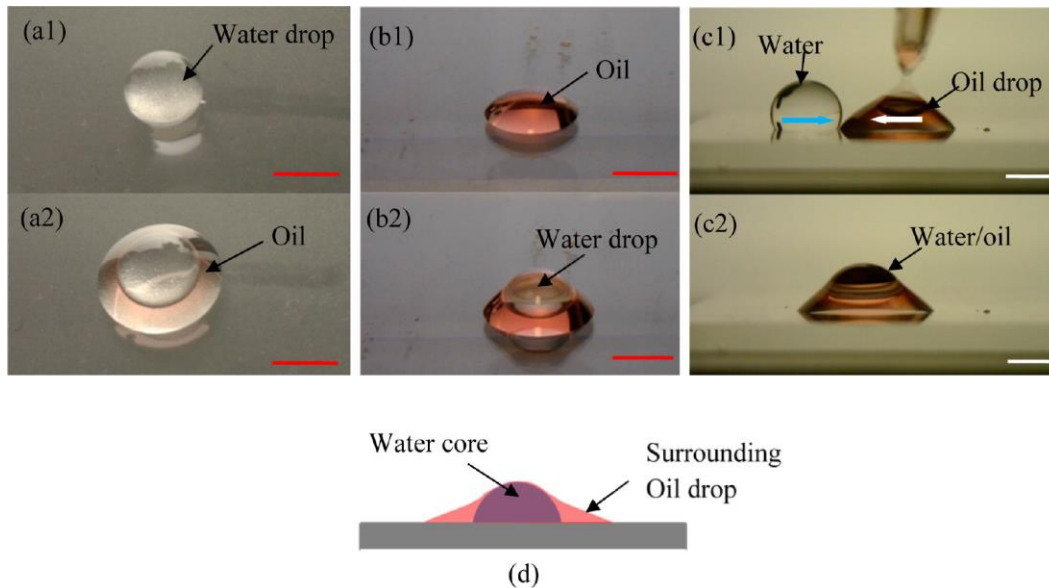
Figure 5.1 A mixed drop that is produced by a 10 µL silicone oil drop and a 10 µL water drop on a Teflon plate (side or perspective view). (a1) A pre-existing water drop, and (a2) the mixed drop that is generated by adding oil on the water drop. (b1) A pre-existing oil drop, and (b2) a water drop is added on the oil drop. (c1) A water drop is first placed on the plate, and an oil drop is then put beside the water drop, and (c2) two drops merge together to form a mixed one after they contact. (d) Cross-sectional schematic of a mixed drop. To facilitate observation, the oil is dyed red. Scale bars represent 2 mm.

5.2.3. Separation procedure

Oil has been separated from a mixed drop on each pair of plates through two squeezing steps (Figs. 5.2-5.4). In both steps, the water core is pinned or may just have a small lateral displacement. However, the part of the oil in the mixed drop flows towards the corner of the two plates. In the first squeezing step (Figs. 5.2(a2), 5.2(b2), 5.3(b), and 5.4(b)), once the top plate is lowered down to have contact with the mixed drop, the majority of the oil moves from the left-hand side of the water core to the right-hand side. In the second squeezing step (Figs. 5.2(a3), 5.2(a4), 5.2(b3), 5.2(b4), 5.3(c), 5.3(d),

5.4(c), and 5.4(d)), when the mixed drop is further pressed by the top plate, the oil breaks up with the water core, forms a separate drop, and continues to move towards the plate corner. Similar breaking phenomena have been previously observed, when a water drop falls down from a needle due to the increase of the drop weight [69], or when a liquid drop is cut into two smaller ones from its middle portion by decreasing contact angles at its two ends using the EWOD [97]. Obviously, the breaking in our case is caused by the reduction in the plate gap.
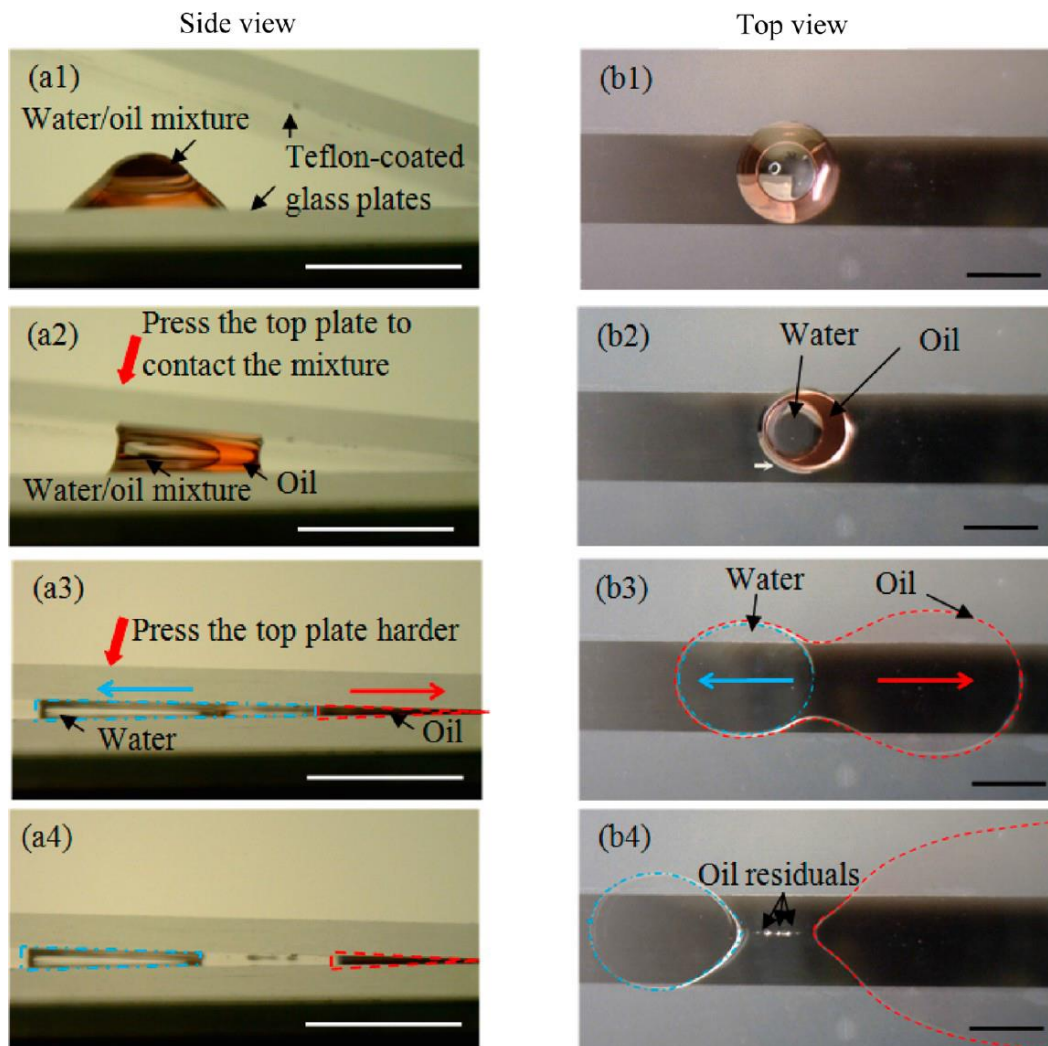
Figure 5.2 (a) Side and (b) top views of the separation process of a water/silicone oil (10 μL/10 μL) mixed drop between two Teflon plates: (a1, b1) the drop is formed on the bottom plate; (a2, b2) part of the oil moves toward the corner of the two plates when the mixture is slightly squeezed; (a3, b3) the water and oil move toward opposite directions when the mixed drop is further pressed; and (a4, b4) the majority of the oil is separated from the original mixed drop, forming a pure oil drop. Scale bars represent 4 mm.
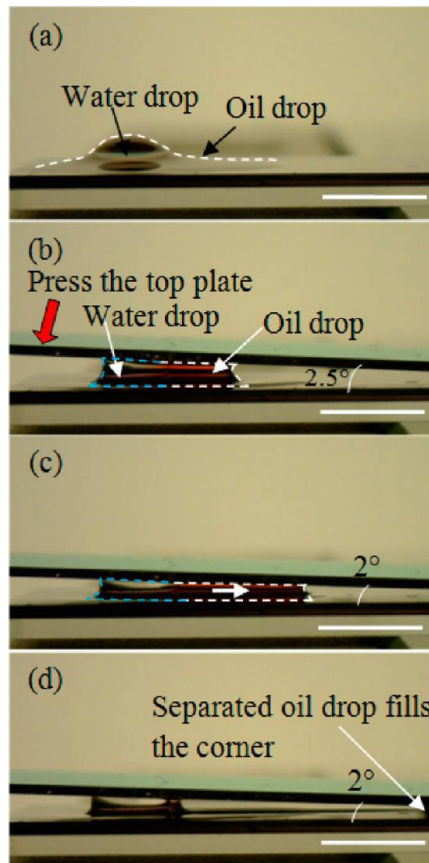
Figure 5.3 Side views of the separation process of a water/silicone oil (10 µL/20 µL) mixed drop between two SiO$_2$ plates: (a) the drop is produced on the surface of bottom plate, (b) part of the oil moves toward the corner of two plates when the drop is slightly squeezed; (c) the oil continuously moves toward the corner, while the water core does not move when the mixed drop is squeezed harder; and (d) the majority of the oil is separated from the drop and fills the plate corner. Scale bars represent 4 mm.
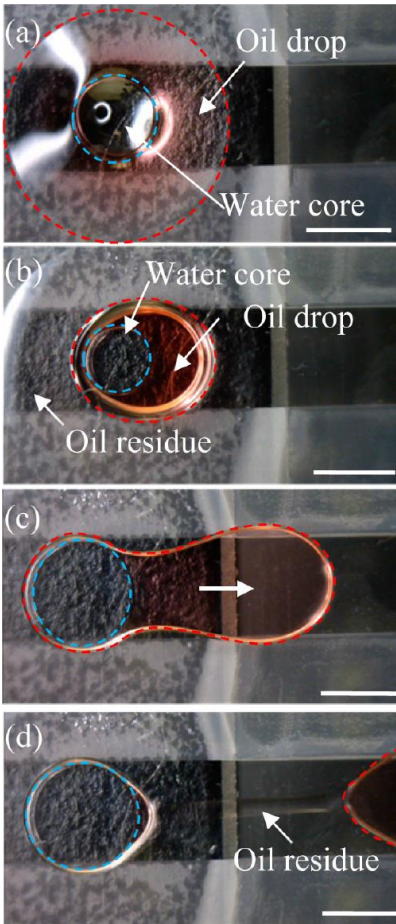
Figure 5.4 Top views of the separation process of a water/silicone oil (10 μL/20 μL) mixed drop between two SU-8 plates: (a) the drop is formed on the bottom plate, (b) part of oil moves toward the corner of two plates when the mixed drop is slightly squeezed; (c) the oil continuously moves toward the plate corner, while the water core does not move when the mixed drop is further squeezed; and (d) oil drop is separated from the water drop, and moves toward the plate corner. Scale bars represent 4 mm.

5.2.4. Collection and the effect of volumes

After the separation, the newly formed oil drop is collected using a capillary tube. In the case of the Teflon plates, its volume is measured to be 9.55 μL. The oil component

in the 20 μL mixed drop initially has a volume of 10 μL. Accordingly, the separation efficiency is 95.5%. Since the contact angles of the oil on another two types of plates are close to 0º, the newly formed oil drops spread on these plates, making it difficult to remove the entire drops from the plates. Thus, for the purpose of collecting more separated oil, the Teflon plates are the best option among the three types of plates.

We further examine the effects of both volumes and volume ratios of mixed drops on critical opening angles. Such an angle refers to upper limit of the opening angles of two plates that are needed to separate a mixed drop. If this angle is small, then it means that the mixed drop has to be deeply pressed to separate the mixture. When the opening angles are larger than the critical ones, separation does not occur. In the tests, water cores in the mixed drops had the volumes of 10, 20 and 30 μL, respectively, while the water/oil ratios varied from 1:1 to 1:4. Fig. 5.5 gives representative results on Teflon plates. Three points are observed from this figure and the testing results on another two types of plates (not shown here). First, the critical opening angles are small, which are all below 5°. Second, when the volume of the water core is fixed, the critical opening angle increases with the increase in the water/oil volume ratio. Third, for a fixed water/oil ratio, the critical opening angle increases with the increase in the total volume of the mixed drop.
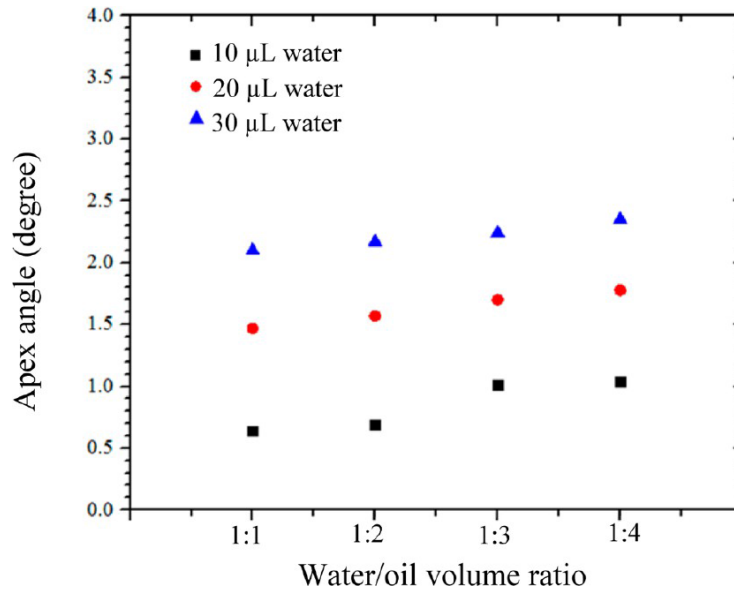
Figure 5.5 Critical opening angles to separate mixed drops using two Teflon plates, when

water and silicone oil have different volume ratios in the drops and the volumes of the

water cores are 10, 20, and 30 µL, respectively.

5.3 Theoretical model

In this section, we first consider pressure difference inside a liquid drop, then derive some relations, and finally use these relations to explain the physical mechanism of the separation process, as well as the observed phenomena, followed by experimental validation and selection of plate coatings.

5.3.1. Pressure difference in a liquid drop

Consider a liquid drop that is located between two fixed plates. This liquid drop may be surrounded by air or another liquid. The bottom plate is oriented horizontally. As illustrated in Fig. 5.6(a), for simplicity, the right and left edges of the liquid drop are called "Edge 1" and "Edge 2," respectively. Use e and α, respectively, to denote apex edge and opening angle of the two plates. Let a_1 and b_1 denote the two points that Edge 1 intersects with the bottom and top plates, separately, and set a_2 and b_2 to be the two

intersecting points that Edge 2 forms with the bottom and top plates, respectively. Use l_p to denote the distance between e and a_1, and set l_l to be the length of a_1a_2. Let p_1 and p_2 represent liquid pressures at Edges 1 and 2, respectively. Set p_{1s} and p_{2s} to denote the pressures of surrounding air or liquid at these two edges, separately.
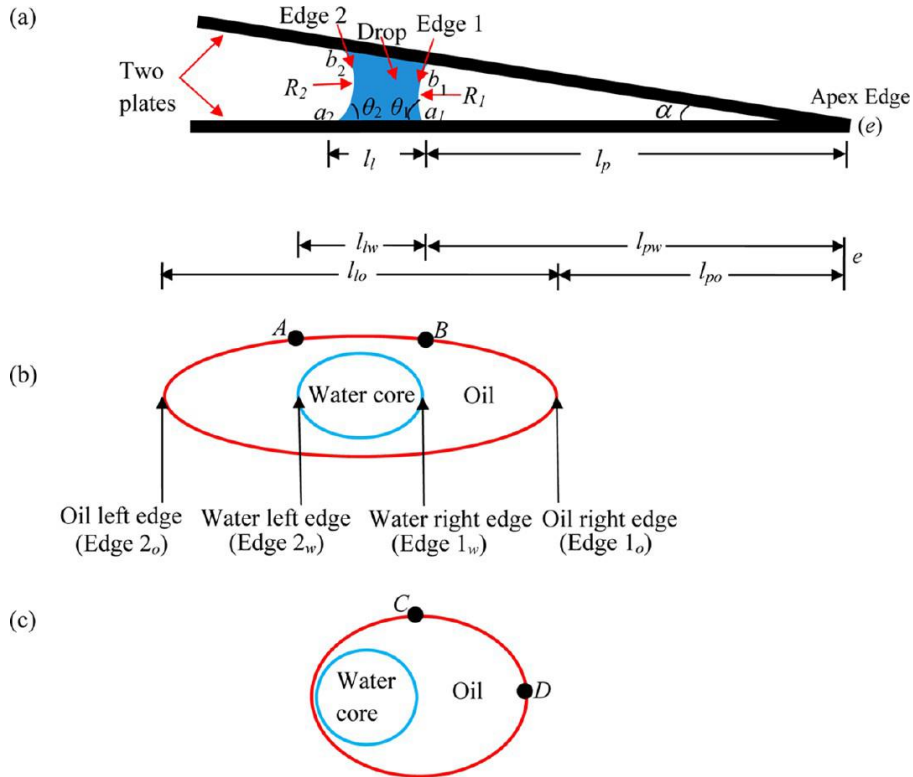
Figure 5.6 (a) Cross-sectional schematic of a liquid drop placed between two nonparallel plates. Top schematics of the water/oil mixed drop between two nonparallel plates when the mixed drop is (b) first slightly pressed and (c) then further squeezed.

In this work, half heights of the pressed liquid drops are less than the capillary length of a liquid, which is 2.7 mm in the case of water. Accordingly, the gravity effect on the liquid pressure is neglected, and p_1 and p_2 are uniform, respectively, on Edges 1 and 2 [23,64,65]. Subsequently, both Edges 1 and 2 are considered to be circular arcs

85

[23]. Use R_1 and R_2 to represent the radii of these two edges, respectively. Let θ_1 represent equilibrium contact angle at a1 and b1, and use θ_2 to stand for the one at a_2 and b_2. Set θ_a and θ_r to be, respectively, advancing and receding contact angles. Then, both θ_1 and θ_2 vary between θ_r and θ_a. It follows from geometric analysis that

$$\frac{1}{R_1} = \frac{\cos(\frac{\alpha}{2} - \theta_1)}{l_p \sin\frac{\alpha}{2}}, \tag{5.1}$$

$$\frac{1}{R_2} = \frac{\cos(\frac{\alpha}{2} + \theta_2)}{(l_p + l_l)\sin\frac{\alpha}{2}}. \tag{5.2}$$

In addition, let R_{12} and R_{22} denote the radii of the curves that are perpendicular to Edges 1 and 2, respectively, on the drop surface. Accordingly, $\frac{1}{R_{12}}$ and $\frac{1}{R_{22}}$ denote the curvatures of these curves. In this work, the plate gap is much smaller than the drop radius. Since R_1 and R_{12} are in the same order as the plate gap and drop radius, respectively, R_1 is considered to be much smaller than R_{12}. Accordingly, in comparison with $\frac{1}{R_1}$, the effect of $\frac{1}{R_{12}}$ on p_1 can be neglected. Likewise, during the consideration of p_2, the effect of $\frac{1}{R_{22}}$ is also neglected. Subsequently, in terms of Young-Laplace equation [68] and with the aid of Eqs. (5.1) and (5.2), p_1 and p_2 are, respectively,

$$p_1 = \frac{-\gamma\cos(\frac{\alpha}{2} - \theta_1)}{l_p \sin\frac{\alpha}{2}} + p_{1s}, \tag{5.3}$$

$$p_2 = \frac{-\gamma\cos(\frac{\alpha}{2}+\theta_2)}{(l_p+l_l)\sin\frac{\alpha}{2}} + p_{2s},\tag{5.4}$$

where γ denotes the surface tension of the interface that the liquid forms with the surrounding air or liquid. By Eqs. (5.3) and (5.4), we have

$$p_2 - p_1 = [\frac{\gamma\cos(\frac{\alpha}{2}-\theta_1)}{l_p\sin\frac{\alpha}{2}} - \frac{\gamma\cos(\frac{\alpha}{2}+\theta_2)}{(l_p+l_l)\sin\frac{\alpha}{2}}] + (p_{2s}-p_{1s}).\tag{5.5}$$

In our tests, α is always less than 5°. Thus, $\cos(\frac{\alpha}{2}-\theta_1)$, $\cos(\frac{\alpha}{2}+\theta_2)$, and $\sin\frac{\alpha}{2}$ can be simplified as $\cos\theta_1$, $\cos\theta_2$, and $\frac{\alpha}{2}$, respectively. Subsequently, it follows from Eq. (5.5) that

$$p_2 - p_1 = \frac{2\gamma}{\alpha}(\frac{\cos\theta_1}{l_p} - \frac{\cos\theta_2}{l_p+l_l}) + (p_{2s}-p_{1s}).\tag{5.6}$$

5.3.2. Three relations

In this sub-section, we apply the basic liquid drop model of Fig. 5.6(a), together with Eq. (5.6), to explain the behaviors of the water and oil during the squeezing process.

We first consider the pressure in the oil component of a mixed drop in the first squeezing step. Denote the left and right edges of the oil as Edges 2_o and 1_o, respectively (Fig. 5.6(b)). The oil portion of the mixed drop is surrounded by air. Thus, both p_{1s} and p_{2s} equal atmospheric pressure. Edges 1_o and 2_o are actually two lines on the oil/air interfaces. Let γ_o be the surface tension of such an interface. Use l_{po} to denote the distance between apex edge and Edge 1_o, and set l_o to be the length of the oil drop. Set p_{1o} and p_{2o} to be the oil pressures at Edges 1_o and 2_o, respectively. Use θ_{1o} and θ_{2o} to represent the equilibrium contact angles at the two edges, separately, and let θ_{ro} and

θ_{ao} be the corresponding receding and advancing contact angles. On the basis of the analogy between the models of the oil and the generic liquid drop, it follows from Eq. (5.6) that

$$p_{2o} - p_{1o} = \frac{2\gamma_o}{\alpha}(\frac{\cos\theta_{1o}}{l_{po}} - \frac{\cos\theta_{2o}}{l_{po} + l_{lo}}) . \tag{5.7}$$

If

$$\theta_{ro} \approx \theta_{ao}, \tag{5.8}$$

$$\theta_{ro} < 90^\circ, \tag{5.9}$$

then it follows from Eq. (5.7) that

$$p_{2o} - p_{1o} = \frac{2\gamma_o\cos\theta_{ro}}{\alpha}(\frac{1}{l_{po}} - \frac{1}{l_{po} + l_{lo}}) > 0. \tag{5.10}$$

Relation (5.8) implies that contact angle hysteresis of the oil is close to 0°. Consequently, both θ_{1o} and θ_{2o} approximately equal θ_{ro}. Ineq. (5.9) further ensures that $\cos\theta_{ro} > 0.$ Accordingly, as shown in relation (5.10), we have $p_{2o} > p_{1o}$. In other words, relations (5.8) and (5.9) actually form a sufficient condition to make p_{2o} always larger than p_{1o}. Due to this pressure difference, the oil moves from Edges 2_o to 1_o. According to the values of θ_{ro} and θ_{ao} given in Table 5.1, relations (5.8) and (5.9) are met on each pair of plates. Hence, in the first step, the oil was observed to flow rightwards in the corresponding test (Figs. 5.2(a2), 5.2(b2), 5.3(b) and 5.4(b)).

We then consider the pressure in the water core during the first squeezing step. Denote the left and right edges of the water core as Edges 2_w and 1_w, respectively (Fig. 5.6b). The water core is surrounded by oil. The two edges are actually two lines on the water/oil interfaces. Let γ_m be the surface tension of a water/oil interface. Use l_{pw} to denote the distance between apex edge and Edge 1_w, and set l_{lw} to be the length of the

water core. Use p_{2w} and p_{1w} to represent the water pressures at Edges 2_w and 1_w, separately. Set θ_{1m} and θ_{2m} to be the equilibrium contact angles at the two edges, respectively, and let θ_{rm} and θ_{am} be the corresponding receding and advancing contact angles. According to the analogy between the models of the water core and the generic liquid drop, it follows from Eq. (5.6) that

$$p_{2w} - p_{1w} = \frac{2\gamma_m}{\alpha}(\frac{\cos\theta_{1m}}{l_{pw}} - \frac{\cos\theta_{2m}}{l_{pw}+l_{lw}}) + (p_{2s} - p_{1s}). \qquad (5.11)$$

In this equation, p_{1s} and p_{2s} equal the oil pressures at Edges 1_w and 2_w, respectively. We use the oil pressures at the oil and air interfaces, which are close to the two edges and are marked as A and B in Fig. 5.6(b), to approximate p_{2s} and p_{1s}. Following the same way applied to derive Eq. (5.7) and making use of relation (5.8), we get

$$p_{2s} - p_{1s} = \frac{2\gamma_o\cos\theta_{ro}}{\alpha}(\frac{1}{l_{pw}} - \frac{1}{l_{pw}+l_{lw}}). \qquad (5.12)$$

With the aid of Eq. (5.12), by Eq. (5.11), we have

$$p_{2w} - p_{1w} = \frac{2\gamma_m}{\alpha}(\frac{\cos\theta_{1m}}{l_{pw}} - \frac{\cos\theta_{2m}}{l_{pw}+l_{lw}}) + \frac{2\gamma_o\cos\theta_{ro}}{\alpha}(\frac{1}{l_{pw}} - \frac{1}{l_{pw}+l_{lw}}). \quad (5.13)$$

Assume that water core also moves towards the plate corner. Then, θ_{1m} and θ_{2m} equal θ_{am} and θ_{rm}, respectively. Subsequently,

$$p_{2w} - p_{1w} = \frac{2\gamma_m}{\alpha}(\frac{\cos\theta_{am}}{l_{pw}} - \frac{\cos\theta_{rm}}{l_{pw}+l_{lw}}) + \frac{2\gamma_o\cos\theta_{ro}}{\alpha}(\frac{1}{l_{pw}} - \frac{1}{l_{pw}+l_{lw}}). \qquad (5.14)$$

Since $(\frac{\cos\theta_{am}}{l_{pw}} - \frac{\cos\theta_{rm}}{l_{pw}+l_{lw}}) \leq \cos\theta_{am}(\frac{1}{l_{pw}} - \frac{1}{l_{pw}+l_{lw}})$, by Eq. (5.14), it is readily shown that, if

$$(\gamma_m\cos\theta_{am} + \gamma_o\cos\theta_{ro}) < 0, \qquad (5.15)$$

then

$$p_{2w} < p_{1w}. \hspace{3cm} (5.16)$$

Consequently, water core cannot move towards corner, because the pressure at Edge 1_w is larger than the one at Edge 2_w. This is against our assumption, and thus results in a contradiction. Therefore, Ineq. (5.15) is a sufficient condition to prevent the water core from moving towards the plate corner during the first squeezing step.

Finally, we consider the second squeezing step. In this step, Ineq. (5.15) still applies to the water core, and the water still does not move towards the plate corner. The part of the oil considered is the one located on the right-hand side of the water core. Consider the oil pressures at the places of C and D, which are marked on Fig. 5.6(c) and, respectively, correspond to Edges 2 and 1 of the liquid drop of Fig. 5.6(a). Relation (5.10) also applies here. Two points can be observed from this relation. First, the pressure difference between C and D increases with the decrease in α, and goes to infinity when α approaches 0. Hence, during the pressing process, the pressure difference can be made high enough to break the part of the oil from the mixed drop. Since the largest pressure difference occurs between C and D, the breaking happens at C. Second, for fixed θ_{ro} and α, the pressure difference also increases with the decrease in l_{po} and the increase in l_{lo}.

The second point actually can be used to explain what has been previously observed from Fig. 5.5. The mixed drops with different volumes but the same water/oil ratios are positioned at the same location of the bottom plate, before they are pressed by the top plate. When these drops are pressed at the same degree, i.e., the corresponding opening angles of the two plates are the same, the values of l_{po} and l_{lo} decrease and increase, respectively, with the increase in the volume. Accordingly, the pressure difference also increases with the increase in the drop volume. This result implies that, when water/oil ratios are fixed, the critical opening angle increases as well with the drop

volume. Likewise, the critical opening angle should also increase with the increase of the oil volume in a drop, which has a fixed amount of water.

In summary, based on the theoretical modeling, once relations (5.8), (5.9) and (5.15) are satisfied, the oil should be separated from the water/oil mixed drop during a squeezing process.

5.3.3. Validation of the three relations

As discussed in the previous sub-section, relations (5.8) and (5.9) have been validated in our tests. Next, we desire to examine whether Ineq. (5.15) is also satisfied. For this purpose, we measure the advancing and receding contact angles on the three types of plates using an approach of reference 98. As shown in Fig. 5.7, a plate is inserted into a mixed solution of water and silicone oil. The oil layer is on the top of the water, since the oil is less dense than water. When the plates are stationary inside the mixed solutions, equilibrium contact angles of the water/oil interfaces on SiO_2, SU-8 and Teflon plates are observed to be, respectively, 115°, 118°, and 148° (Fig. 5.7). Meanwhile, it is also noted that the equilibrium contact angle of the water/oil interface on FC725-coated glass fibers is large, which was reported to be about 143° [98]. The advancing and receding angles of the water/oil interface on a place are measured by slightly moving the plate up and down in the solution. As predicted using Ineq. (5.15), the values of θ_{am} on SiO_2, SU-8 and Teflon plates are greater than 90°, which are measured to be 158°, 165°, and 155°, respectively (not shown in Fig. 5.7). The corresponding values of θ_{rm} are 112°, 106°, and 141°.
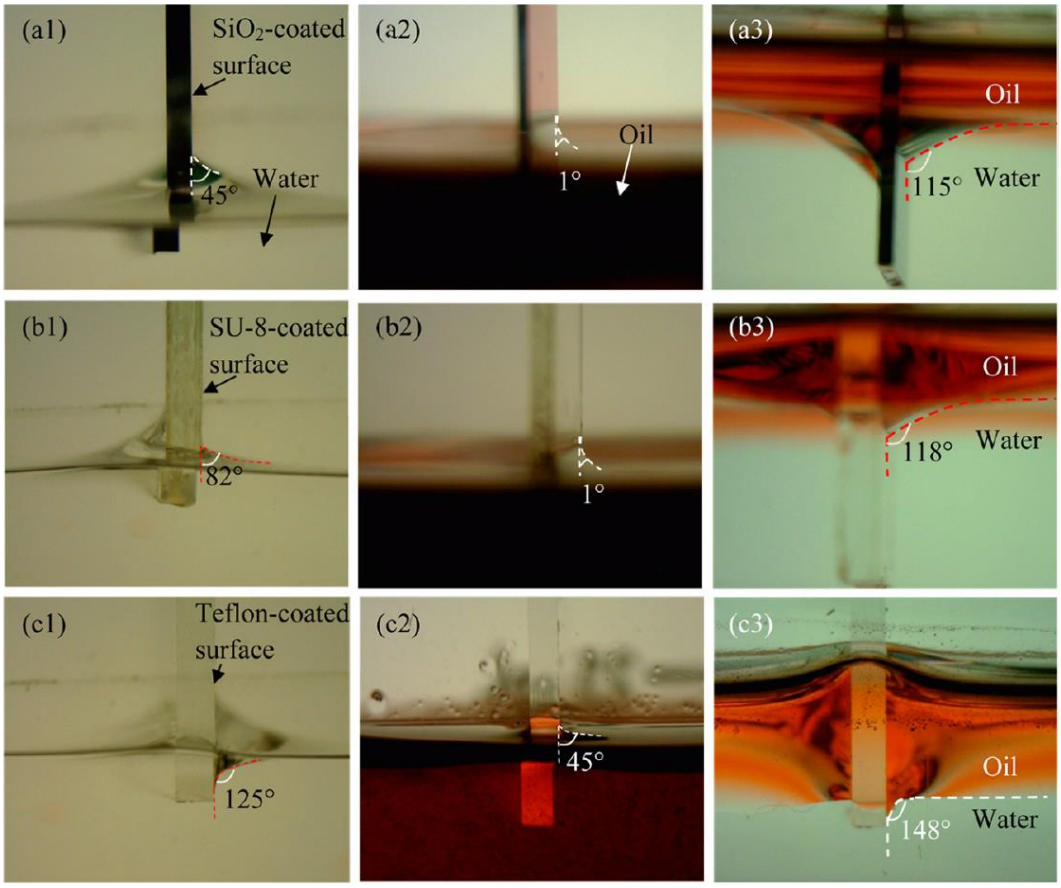
Figure 5.7 Measurement of contact angles on (a) SiO$_2$, (b) SU-8, and (c) Teflon plates when these plates are inserted into solutions. The wetting situations of (a1, b1, c1) water, (a2, b2, c2) silicone oil, and (a3, b3, c3) water/silicone oil on the three plates. The error of the angle measurement is 2°.

In addition, the corresponding contact angles of oil and water on the plates with different coatings are also measured by inserting the plates, respectively, into pure oil and water solutions (Fig. 5.7). Equilibrium contact angles on stationary SiO$_2$, SU-8 and Teflon plates are observed to be, respectively, 45°, 82°, and 125° in the case of water solutions, while they are 1°, 1°, and 45° for the case of oil solutions (Fig. 5.7). The

advancing and receding angles that are subsequently detected are close to the ones given in Sub-section 5.2.1 (Table 5.1).

It is reported in reference 98 (see its Table 1) that surface tension of silicone oil is about 18.4 dynes/cm, and that the interfacial tension between water and silicone oil is around 40.3 dynes/cm. Based on these data, together with the values of contact angles, Ineq. (5.15) is satisfied in the test on each pair of plates.

5.3.4. Separation of another mixture

To further validate the three relations, we also explore the possibility of separating light mineral oil (Sigma-Aldrich Co., MO, USA) from its mixture with water. The advancing contact angles of this oil on Teflon, SiO_2 and SU-8 plates are measured to be 62°, 16° and 27°, respectively, while the receding contact angles are 60°, 15° and 27° (Table 5.1). The advancing contact angles of the water/oil interfaces on the SiO_2, SU-8 and Teflon plates are 155°, 154° and 158°, separately, while the receding contact angles on these three plates are 133°, 116° and 147°. Meanwhile, the surface tension of light mineral oil and the interfacial tension between water and light mineral oil are reported to be slightly below 35 [99] and 49.3 dynes/cm [100], respectively, at 25 ^{o}C. According to these data, relations (5.8), (5.9) and (5.15) are satisfied. Accordingly, in the subsequent tests, the mixture has been successfully separated using each of the three pairs of plates. After the separation, the newly formed oil drop is collected using a capillary tube. Due to different contact angles of light mineral oil on the three types of plates (Table 5.1), the separation efficiencies on SU-8 and Teflon plates are 96.2% and 97.0%, respectively. In addition, since the contact angle of light mineral oil on the SiO_2 plate is as small as 15°, the newly formed oil drop spreads on this plate, making it difficult to remove the entire drop from the plate. Different from that in the case of silicone oil, both SU-8 and Teflon plates are good options for collecting the separated light mineral oil.

The mass density of light mineral oil is 838 Kg/m^3 at 25 $^\text{o}$C. It is also noted that the mixture has a profile similar to the one given in Fig. 5.1(d). The viscosities of silicone oil and light mineral oil are 40 and 20 mm^2/s, respectively, while that of water is only 1 mm^2/s. According to relations (5.8), (5.9) and (5.15), whether a mixture could be separated does not depend on the viscosities of the two liquids. Therefore, although there is a large difference between the viscosities of water and oil, their mixture is still separated. On the other hand, a high viscosity means a large force to resist a liquid flow. Accordingly, the separation time should increase with the increase in the viscosity. In our case, due to the short moving distance of liquid drops, all the separations are accomplished within 2 min. Consequently, the effect of the oil viscosity on the separation time is not specifically considered.

5.3.5. Selection of a plate coating

Relations (5.8), (5.9) and (5.15) indicate that, to enable the developed approach to separate a mixed drop, a critical point is to find a good plate coating. This coating should meet the following four requirements. First, the liquid with lower mass density should be lyophilic on the coating, and its contact angle hysteresis should be close to 0$^\text{o}$. A drop of this liquid will be separated from the mixed one. To make it easy to collect the separated drop, the contact angle of the liquid on the coating should be relatively large, which is the second requirement. Third, the interface of the two liquids should form an angle greater than 90$^\text{o}$ with this coating. Fourth and finally, this angle, together with the receding contact angle of the liquid with lower mass density, should make Ineq. (5.15) hold true.

In the cases of water/silicone oil and water/light mineral oil, all the three coatings explored here meet the first, third and fourth requirement. However, the Teflon coating is the only one which also satisfies the second requirement in the case of water/silicone oil,

while both SU-8 and Teflon coatings meet this requirement for the case of water/light mineral oil.

In this work, all the plates used have flat surfaces. Instead of employing coatings, wetting properties on the plates can also be changed by modifying the plate surfaces using micro- or nanostructures [83,84,87,23]. However, this modification method may not be suited at separating a mixture. By Ineq. (5.9), the oil should wet the substrate. Thus, once it contacts roughness structures, it penetrates into the grooves between them [23], making the oil pinned on the structures. Due to this pinning effect, it is difficult to separate the oil from the mixture in the squeezing process. Also, even if it might be separated, not much oil would be collected, since the oil is trapped inside the roughness structures.

5.4 Summary and conclusions

In this work, we developed a new approach to separate a µL-scaled mixed drop of two immiscible liquids through experimental and theoretical investigations. This approach makes use of different wetting properties of the two liquids. Water, silicone oil and light mineral oil have been selected as representative liquids for exploring the new approach. Three pairs of non-parallel plates with different coatings have been used to separate the mixed drops of these two liquids. Based on experimental tests, three theoretical relations, which are (5.8), (5.9) and (5.15), have been derived. As validated by experimental results, these relations form a sufficient condition for the separation to occur. Although only water and two oils are considered in this work, given that the three theoretical relations are satisfied, the developed approach may also be applied to separate another pair of immiscible liquids. To make these relations hold true, the critical point is to find a good plate coating. As discussed in Sub-section 5.3.5, this coating should meet four requirements.

Chapter 6

Conclusion and Summary

In this dissertation, we first investigated the behaviors of liquid drops on conical wires and developed a cactus-inspired fog collector. We then explored the motions of liquid drops between two nonparallel plates. Based on the corresponding mechanisms, we further generated a shorebird-motivated fog collector and developed an approach to separate oil from water/oil mixed drop on the basis of two nonparallel plates.

First, we have developed an artificial branched wire structure to harvest water from fog and dew. Vapor-Solid approach is applied to synthesize such a structure. As in the case of the cactus, all these wires in this structure have conical shapes, yielding a capillary force to drive a water drop to move from the tip of a wire to the root. On the other hand, due to relatively larger surface areas of the branched wires in the artificial structure, this structure collected more water in comparison with the cactus structure. In addition, it is also found that the amount of water collected is related to the direction of the incoming vapor flow. Furthermore, we have demonstrated that, with the aid of a syringe, large drops located at the root of a branched wire structure can be pumped into a glass tube, making this structure capable of continuously collecting water.

Second, through the comparison of the liquid pressures on two opposite edges of a liquid drop, together with the consideration of contact angle hysteresis, we have considered four possible cases, and identified whether a liquid drop fills the corner of two nonparallel plates in each case. We have also developed two approaches that may enable an initially stationary drop to fill the corner. Furthermore, we have proposed a model to interpret the shifting effect of a liquid drop when it is squeezed and relaxed between two non-parallel plates. Three new phenomena were predicted based on this model, which were subsequently validated by two experiments.

Third, based on the gained understandings of the feeding mechanism of a shorebird, we have developed a plate-based collector to harvest water from fog and dew. As in the case of the shorebird, squeezing and relaxing processes have been applied to facilitate the transport of condensed water drops from the plate surfaces to the corner of two plates. We have explored the condensation and collection of a small version of the artificial collector, and found it was much efficient than desert animal and plants due to the active transport of condensed water, which ensured that all the water condensed on the artificial collector was almost collected. Based on these results, we further developed a large collector. Because of its relatively larger surface areas, 15.8 mL water was collected during a condensation period of 36 min.

Finally, by using two nonparallel plates, we developed a new approach to separate a μL-scaled mixed drop of two immiscible liquids through experimental and theoretical investigations. This approach makes use of different wetting properties of the two liquids. Based on experimental tests, three theoretical relations, which are (5.8), (5.9) and (5.15), have been derived. As validated by experimental results, these relations form a sufficient condition for the separation to occur. Although only water and two oils are considered in this work, given that the three theoretical relations are satisfied, the developed approach may also be applied to separate another pair of immiscible liquids. To make these relations hold true, the critical point is to find a good plate coating. As discussed in Sub-section 5.3.5, this coating should meet four requirements.

References

(1)   Middleton, N. Deserts: A Very Short Introduction; Oxford University Press: New York, 2009; pp 4, 16, 19.

(2)   Parker, A. R.; Lawrence, C. R. Water capture by a desert beetle *Nature* 2001, 414, 33-34.

(3)   Ju, J.; Bai, H.; Zheng, Y.; Zhao, T.; Fang, R.; Jiang, L. A multi-structural and multi-functional integrated fog collection system in cactus *Nat. Commun.* 2012, 3, 1247.

(4)   Ebner, M.; Miranda, T.; Roth-Nebelsick, A. Efficient fog harvesting by Stipagrostis sabulicola (Namib dune bushman grass) *J. Arid Environ.* 2011, 75, 524-531.

(5)   Andrews, H.; Eccles, E.; Schofield, W.; Badyal, J. Three-dimensional hierarchical structures for fog harvesting *Langmuir* 2011, 27, 3798-3802.

(6)   Lorenceau, É.; Quéré, D. Drops on a conical wire *J. Fluid Mech.* 2004, 510, 29-45.

(7)   Zheng, Y.; Bai, H.; Huang, Z.; Tian, X.; Nie, F.-Q.; Zhao, Y.; Zhai, J.; Jiang, L. Directional water collection on wetted spider silk *Nature* 2010, 463, 640-643.

(8)   Zhai, L.; Berg, M. C.; Cebeci, F. C.; Kim, Y.; Milwid, J. M.; Rubner, M. F.; Cohen, R. E. Patterned superhydrophobic surfaces: toward a synthetic mimic of the Namib Desert beetle *Nano Lett.* 2006, 6, 1213-1217.

(9)   Garrod, R.; Harris, L.; Schofield, W.; McGettrick, J.; Ward, L.; Teare, D.; Badyal, J. Mimicking a stenocara beetle's back for microcondensation using plasmachemical patterned superhydrophobic-superhydrophilic surfaces *Langmuir* 2007, 23, 689-693.

(10)   Dorrer, C.; Rühe, J. r. Mimicking the Stenocara Beetle Dewetting of Drops from a Patterned Superhydrophobic Surface *Langmuir* 2008, 24, 6154-6158.

(11)   Thickett, S. C.; Neto, C.; Harris, A. T. Biomimetic surface coatings for atmospheric water capture prepared by dewetting of polymer films *Adv. Mater.* 2011, 23, 3718-3722.

(12)   Nørgaard, T.; Ebner, M.; Dacke, M. Animal or plant: which is the better fog water collector? *PLoS One* 2012, 7, e34603.

(13)   Ju, J.; Xiao, K.; Yao, X.; Bai, H.; Jiang, L. Bioinspired Conical Copper Wire with Gradient Wettability for Continuous and Efficient Fog Collection *Adv. Mater.* 2013, 25, 5937-5942.

(14)   Domen, J. K.; Stringfellow, W. T.; Camarillo, M. K.; Gulati, S. Fog water as an alternative and sustainable water resource *Clean Technol. Environ. Policy* 2014, 16, 235-249 .

(15)   Park, W.; Yi, G.-C.; Kim, J.-W.; Park, S.-M. Schottky nanocontacts on ZnO nanorod arrays *Appl. Phys. Lett.* 2003, 82, 4358-4360.

(16)   Park, W. I.; Kim, J. S.; Yi, G.-C.; Bae, M.; Lee, H.-J. Fabrication and electrical characteristics of high-performance ZnO nanorod field-effect transistors *Appl. Phys. Lett.* 2004, 85, 5052-5054.

(17)   Kind, H.; Yan, H.; Messer, B.; Law, M.; Yang, P. Nanowire ultraviolet photodetectors and optical switches *Adv. Mater.* 2002, 14, 158-160.

(18)   Wang, X.; Summers, C. J.; Wang, Z. L. Large-scale hexagonal-patterned growth of aligned ZnO nanorods for nano-optoelectronics and nanosensor arrays *Nano Lett.* 2004, 4, 423-426.

(19)   Vispute, R.; Talyansky, V.; Choopun, S.; Sharma, R.; Venkatesan, T.; He, M.; Tang, X.; Halpern, J.; Spencer, M.; Li, Y. Heteroepitaxy of ZnO on GaN and its

implications for fabrication of hybrid optoelectronic devices *Appl. Phys. Lett.* 1998, 73, 348-350.

(20)   Feng, X.; Feng, L.; Jin, M.; Zhai, J.; Jiang, L.; Zhu, D. Reversible super-hydrophobicity to super-hydrophilicity transition of aligned ZnO nanorod films *J. Am. Chem. Soc.* 2004, 126, 62-63.

(21)   Wang, Z. L.; Song, J. Piezoelectric nanogenerators based on zinc oxide nanowire arrays *Science* 2006, 312, 242-246.

(22)   Wang, X.; Song, J.; Liu, J.; Wang, Z. L. Direct-current nanogenerator driven by ultrasonic waves *Science* 2007, 316, 102-105.

(23)   Luo, C.; Xiang, M.; Heng, X. A stable intermediate wetting state after a water drop contacts the bottom of a microchannel or is placed on a single corner *Langmuir* 2012, 28, 9554-9561.

(24)   Luo, C. and Xiang M. Angle inequality for judging the transition from Cassie–Baxter to Wenzel states when a water drop contacts bottoms of grooves between micropillars *Langmuir* 2012, 28, 13636-13642.

(25)   Zhang, Y.; Yu, K.; Jiang, D.; Zhu, Z.; Geng, H.; Luo, L. Zinc oxide nanorod and nanowire for humidity sensor *Appl. Surf. Sci.* 2005, 242, 212-217.

(26)   Fan, Z.; Wang, D.; Chang, P.-C.; Tseng, W.-Y.; Lu, J. G. ZnO nanowire field-effect transistor and oxygen sensing property *Appl. Phys. Lett.* 2004, 85, 5923-5925.

(27)   Fan, Z.; Lu, J. G. Gate-refreshable nanowire chemical sensors *Appl. Phys. Lett.* 2005, 86, 123510- 123510-3.

(28)   Liu, T.-Y.; Liao, H.-C.; Lin, C.-C.; Hu, S.-H.; Chen, S.-Y. Biofunctional ZnO nanorod arrays grown on flexible substrates *Langmuir* 2006, 22, 5804 -5809.

(29)   Wen, L.; Wong, K. M.; Fang, Y.; Wu, M.; Lei, Y. Fabrication and characterization of well-aligned, high density ZnO nanowire arrays and their realizations in Schottky device applications using a two-step approach *J. Mater. Chem.* 2011, 21, 7090-7097.

(30)   Xiang, M.; Wilhelm, A.; Luo, C. Existence and role of large micropillars on the leaf surfaces of the president lotus *Langmuir* 2013, 29, 7715-7725.

(31)   Conley Jr, J.; Stecker, L.; Ono, Y. Directed assembly of ZnO nanowires on a Si substrate without a metal catalyst using a patterned ZnO seed layer *Nanotechnology* 2005, 16, 292-296.

(32)   Chakraborty, A.; Liu, X.; Wang, H.; Luo, C. Generation of ZnO nanowires with varied densities and lengths by tilting a substrate *Microsyst. Technol.* 2012, 18, 1497-1506.

(33)   Dalal, S.; Baptista, D.; Teo, K.; Lacerda, R.; Jefferson, D.; Milne, W. Controllable growth of vertically aligned zinc oxide nanowires using vapour deposition *Nanotechnology* 2006, 17, 4811-4818.

(34)   Huang, M. H.; Wu, Y.; Feick, H.; Tran, N.; Weber, E.; Yang, P. Catalytic growth of zinc oxide nanowires by vapor transport *Adv. Mater.* 2001, 13, 113-116.

(35)   Greene, L. E.; Law, M.; Tan, D. H.; Montano, M.; Goldberger, J.; Somorjai, G.; Yang, P. General route to vertical ZnO nanowire arrays using textured ZnO seeds *Nano Lett.* 2005, 5, 1231-1236.

(36)   Hsu, J. W.; Tian, Z. R.; Simmons, N. C.; Matzke, C. M.; Voigt, J. A.; Liu, J. Directed spatial organization of zinc oxide nanorods *Nano Lett.* 2005, 5, 83-86.

(37)   Cheng, C.; Fan, H. J. Branched nanowires: Synthesis and energy applications *Nano Today* 2012, 7, 327-343.

(38)   Bierman, M. J.; Jin, S. Potential applications of hierarchical branching nanowires in solar energy conversion *Energy Environ. Sci.* 2009, 2, 1050-1059.

(39)   Qiu, J.; Li, X.; Zhuge, F.; Gan, X.; Gao, X.; He, W.; Park, S.-J.; Kim, H.-K.; Hwang, Y.-H. Solution-derived 40 µm vertically aligned ZnO nanowire arrays as photoelectrodes in dye-sensitized solar cells *Nanotechnology* 2010, 21, 195602-195610.

(40)   Fan, H.; Fleischer, F.; Lee, W.; Nielsch, K.; Scholz, R.; Zacharias, M.; Gösele, U.; Dadgar, A.; Krost, A. Patterned growth of aligned ZnO nanowire arrays on sapphire and GaN layers *Superlattices Microstruct.* 2004, 36, 95-105.

(41)   Sze, S. VLSI technology, 2nd ed.; McGraw-Hill: New York, 1988.

(42)   Schlichting, H.; Gersten, K. Boundary-layer theory; Springer: Berlin Heidelberg, 2000.

(43)   Wang, M. C.; Gates, B. D. Directed assembly of nanowires *Mater. Today* 2009, 12, 34-43.

(44)   Chang, P.-C.; Fan, Z.; Wang, D.; Tseng, W.-Y.; Chiou, W.-A.; Hong, J.; Lu, J. G. ZnO nanowires synthesized by vapor trapping CVD method *Chem. Mater.* 2004, 16, 5133-5137.

(45)   Nobel, P. S. ed.; Cacti: biology and uses; University of California Press: Berkeley and Los Angeles, CA, 2002; pp 23-27.

(46)   Slatyer, R. O. Absorption of water by plants *Bot. Rev.* 1960, 26, 331-392.

(47)   Franke, W. Mechanisms of foliar penetration of solutions *Annu. Rev.* Plant Physiol. 1967, 18, 281-300.

(48)   Govindjee ed.; Photosynthesis V2: Development, Carbon Metabolism, and Plant Productivity; Academic Press: New York, 1982.

(49)   McCuan, J. Symmetry via spherical reflection and spanning drops in a wedge *Pacific J. Math.* 1997, 180, 291-323.

(50)   Concus, P.; Finn, R. Discontinuous behavior of liquids between parallel and tilted plates *Phys. Fluids* 1998, 10, 39-43.

(51)   Prakash, M.; Quéré, D.; Bush, J. W. Surface Tension Transport of Prey by Feeding Shorebirds: The Capillary Ratchet *Science* 2008, 320, 931-934.

(52)   Taylor, B. Part of a Letter from Mr. Brook Taylor, FRS to Dr. Hans Sloane RS Secr. Concerning the Ascent of Water between Two Glass Planes *Phil. Trans.* 1710, 538-538.

(53)   Concus, P.; Finn, R. On the behavior of a capillary surface in a Wedge *Proc. Natl. Acad. Sci.* USA 1969, 63, 292.

(54)   Concus, P.; Finn, R. On capillary free surfaces in the absence of gravity *Acta. Math.* 1974, 132, 177.

(55)   Concus, P.; Finn, R. "Capillary surfaces in microgravity," in Low-Gravity Fluid Dynamics and Transport Phenomena *Progress in Astronautics and Aeronautics*, edited by J. N. Koster and R. L. Sani, AIAA, Washington, DC, 1990, 130, 183.

(56)   Concus, P.; Finn, R.; McCuan, J. Liquid bridges, edge blobs, and Sherk-type capillary surfaces *Indiana Univ. Math. J.* 2001, 50, 411.

(57)   Weislogel, M. M.; Lichter, S. Capillary flow in an interior corner *J. Fluid Mech.* 1998, 373, 349-378.

(58)   Yuan, Q.; Zhao, Y.P. Topology-dominated dynamic wetting of the precursor chain in a hydrophilic interior corner *Proc. R. Soc. A* 2012, 468, 310-322.

(59)   Bush, J. W.; Peaudecerf, F.; Prakash, M.; Quéré, D. On a tweezer for droplets *Adv. Colloid Interface Sci.* 2010, 161, 10-14.

(60) Rubega, M. A.; Obst, B. S. Surface-tension feeding in phalaropes: discovery of a novel feeding mechanism *The Auk* 1993, 110, 169-178.

(61) Estrella, S. M.; Masero, J. A.; Pérez-Hurtado, A.; Hepp, G. Small-prey profitability: field analysis of shorebirds' use of surface tension of water to transport prey *The Auk* 2007, 124, 1244-1253.

(62) Rubega, M. A. Surface tension prey transport in shorebirds: how widespread is it? *Ibis* 1997, 139, 488-493.

(63) Zweers, G. Transformation of avian feeding mechanisms: a deductive method *Acta. Biotheor.* 1991, 39, 15-36.

(64) Lafuma, A.; Quéré, D. Superhydrophobic states *Nat. Mater.* 2003, 2, 457-460.

(65) Jung, Y.; Bhushan, B. Wetting behavior during evaporation and condensation of water microdroplets on superhydrophobic patterned surfaces *J. Microsc.* 2008, 229, 127-140.

(66) Luo, C.; Xiang, M.; Liu, X.; Wang, H. Transition from Cassie-Baxter to Wenzel States on microline-formed PDMS surfaces induced by evaporation or pressing of water droplets *Microfluid. Nanofluid.* 2011, 10, 831-842.

(67) Marmur, A. A Guide to the Equilibrium Contact Angle Maze *Contact Angle Wettability and Adhesion* 2009, 6, 3.

(68) Adamson, A. W. Physical Chemistry of Surfaces, 5th ed.. John Wiley & Sons: New York, 1990.

(69) de Gennes, P.-G.; Brochard-Wyart, F.; Quéré, D. Capillarity and wetting phenomena: Drops, bubbles, pearls, waves; Springer: Berlin, 2004.

(70) Luo, C.; Xiang, M. Wetting States on Circular Micropillars with Convex Sidewalls after Liquids Contact Groove Base *Langmuir*, 2013, 29, 15065-15075.

(71)   Luo, C.; Xiang, M. Existence and Stability of an Intermediate Wetting State on Circular Micropillars *Microfluid. Nanofluid.* (in press, available on the journal website).

(72)   Qiao, L. and Luo, C. Propulsion of a micro submarine using a thermally oscillatory approach *J. Micromech. Microeng.* 2013, 23, 105011.

(73)   Heng, X.; Xiang, M.; Lu, Z.; Luo, C. Branched ZnO Wire Structures for Water Collection Inspired by Cacti *ACS Appl. Mater. Interfaces* 2014, 6, 8032−8041.

(74)   Cao, M.; Ju, J.; Li, K.; Dou, S.; Liu, K.; Jiang, L. Facile and Large-Scale Fabrication of a Cactus-Inspired Continuous Fog Collector *Adv. Funct. Mater.* 2014, 24, 3235−3240.

(75)   Luo, C.; Heng, X.; Xiang, M. Behavior of a Liquid Drop Between Two Nonparallel Plates *Langmuir* 2014, 30, 8373−8380.

(76)   Viovy, J. L.; Beysens, D.; Knobler, C. M. Scaling Description for the Growth of Condensation Patterns on Surfaces *Phys. Rev. A* 1988, 37, 4965.

(77)   Narhe, R.; Beysens, D. Nucleation and Growth on a Superhydrophobic Grooved Surface *Phys. Rev. Lett.* 2004, 93, 076103.

(78)   Schemenauer, R. S.; Cereceda, P. A Proposed Standard Fog Collector for Use in High-Elevation Regions *J. Appl. Meteorol.* 1994, 33, 1313−1322.

(79)   Kim, G.-T.; Gim, S.-J.; Cho, S.-M.; Koratkar, N.; Oh, I.-K. Wetting-Transparent Graphene Films for Hydrophobic Water- Harvesting Surfaces *Adv. Mater.* 2014, 26, 5166−5172.

(80)   Lee, A.; Moon, M.-W.; Lim, H.; Kim, W.-D.; Kim, H.-Y. Water Harvest via Dewing *Langmuir* 2012, 28, 10183−10191.

(81)   Lee, C.; Baik, S. Vertically-aligned carbon nano-tube membrane filters with superhydrophobicity and superoleophilicity *Carbon* 2010, 48, 2192-2197.

(82)   Shi, Z.; Zhang, W.; Zhang, F.; Liu, X.; Wang, D.; Jin, J.; Jiang, L. Ultrafast Separation of Emulsified Oil/Water Mixtures by Ultrathin Free-Standing Single-Walled Carbon Nanotube Network Films *Adv. Mater.* 2013, 25, 2422-2427.

(83)   Xue, Z.; Wang, S.; Lin, L.; Chen, L.; Liu, M.; Feng, L.; Jiang, L. A Novel Superhydrophilic and Underwater Superoleophobic Hydrogel-Coated Mesh for Oil/Water Separation *Adv. Mater.* 2011, 23, 4270–4273.

(84)   Yang, J.; Zhang, Z.; Xu, X.; Zhu, X.; Men, X.; Zhou, X. Superhydrophilic–superoleophobic coatings *J. Mater. Chem.* 2012, 22, 2834-2837.

(85)   Zhang, X.; Zhang, T.; Ng, J.; Sun, D. D. High‐Performance Multifunctional TiO2 Nanowire Ultrafiltration Membrane with a Hierarchical Layer Structure for Water Treatment *Adv. Funct. Mater.* 2009, 19, 3731-3736.

(86)   Huang, X.; Lim, T.-T. Performance and mechanism of a hydrophobic–oleophilic kapok filter for oil/water separation *Desalination* 2006, 190, 295-307.

(87)   Zhang, F.; Zhang, W. B.; Shi, Z.; Wang, D.; Jin, J.; Jiang, L. Nanowire-Haired Inorganic Membranes with Superhydrophilicity and Underwater Ultralow Adhesive Superoleophobicity for High-Efficiency Oil/Water Separation *Adv. Mater.* 2013, 25, 4192-4198.

(88)   Psillakis, E.; Kalogerakis, N. Developments in liquid-phase microextraction *TrAC, Trends Anal. Chem.* 2003, 22, 565-574.

(89)   Pedersen-Bjergaard, S.; Rasmussen, K. E. Liquid-liquid-liquid microextraction for sample preparation of biological fluids prior to capillary electrophoresis *Anal. Chem.* 1999, 71, 2650-2656.

(90)   Wijethunga, P. A.; Nanayakkara, Y. S.; Kunchala, P.; Armstrong, D. W.; Moon, H. On-chip drop-to-drop liquid microextraction coupled with real-time concentration monitoring technique *Anal. Chem.* 2011, 83, 1658-1664.

(91)   Lorenz H, Despont M and Renaud P 1998 Fabrication of photoplastic high-aspect ratio micro parts and micromolds using SU-8 UV resist *Microsyst. Technol.* 4 143-146.

(92)   Luo, C.; Li, H.; Liu, X. Propulsion of microboats using isopropyl alcohol as a propellant *J. Micromech. Microeng.* 2008, 18, 067002.

(93)   Luo, C.; Qiao, L.; Li, H. Dramatic squat and trim phenomena of mm-scaled SU-8 boats induced by Marangoni effect *Microfluid. Nanofluid.* 2010, 9, 573-577.

(94)   Qiao, L.; Xiao, D.; Lu, F. K.; Luo, C. Control of the radial motion of a self-propelled microboat through a side rudder *Sens. Actuators, A* 2012, 188, 359-366.

(95)   Li, H.; Qiao, L.; Liu, X.; Luo, C. Fabrication and testing of a self-propelled, miniaturized PDMS flotilla *Microsyst. Technol.* 2012, 18, 1431-1444.

(96)   Li, H.; Luo, C. Development of a self-propelled microflotilla *Microsyst. Technol.* 2011, 17, 777-786.

(97)   Cho, S. K.; Moon, H.; Kim, C.-J. Creating, Transporting, Cutting, and Merging Liquid Droplets by Electrowetting-Based Actuation for Digital Microfluidic Circuits *J. Microelectromech. Syst.* 2003, 12, 70-80.

(98)   Gu, Y.; Li, D. Measurements of Contact Angles between an Oil–Water Interface and a Fiber by the ACDPAC Technique *J. Colloid Interface Sci.* 1998, 206, 288–296.

(99)   Xenexlabs (Surface tension of light mineral oil from one of its providers). https://www.xenexlabs.com/catalogue.php?cid=5&pid=1093, accessed on July 3, 2014.

(100)   Stan, C. A.; Tang, S. K. Y.; Whitesides, G. M. Independent Control of Drop Size and Velocity in Microfluidic Flow-Focusing Generators Using Variable

Temperature and Flow Rate *Anal. Chem.* 2009, 81, 2399-2402 (see its supporting information).

Biographical Information

Xin Heng received his B.S. degree in June 2008 from Mechanical and Electronic Control Engineering Institute at Beijing Jiaotong University (BJTU) in China. During his undergraduate studies, he worked in Vehicle Structure Design and System Reliability Lab as a research assistant to contribute to the preliminary work of fatigue tests for the wheel set, frame, and body of 300 km/h high speed passenger locomotive. His Bachelor's thesis is regarding analysis and optimization of the stability and vertical stiffness of large underframe of depressed center flat car. Since the fall of 2010, he has been a Ph.D student in the Mechanical and Aerospace Engineering Department at the University of Texas at Arlington. His research interests are mainly related to biomimetic design, surfaces and colloids, and fluid motion. In the future, he would like to pursue a career in thin film industry.